Supplement of Atmos. Chem. Phys., 16, 5063–5073, 2016
http://www.atmos-chem-phys.net/16/5063/2016/
doi:10.5194/acp-16-5063-2016-supplement

Atmospheric Chemistry and Physics Open Access

Supplement of

Aerosol optical depth trend over the Middle East

Klaus Klingmüller et al.

Correspondence to: Klaus Klingmüller (k.klingmueller@mpic.de)

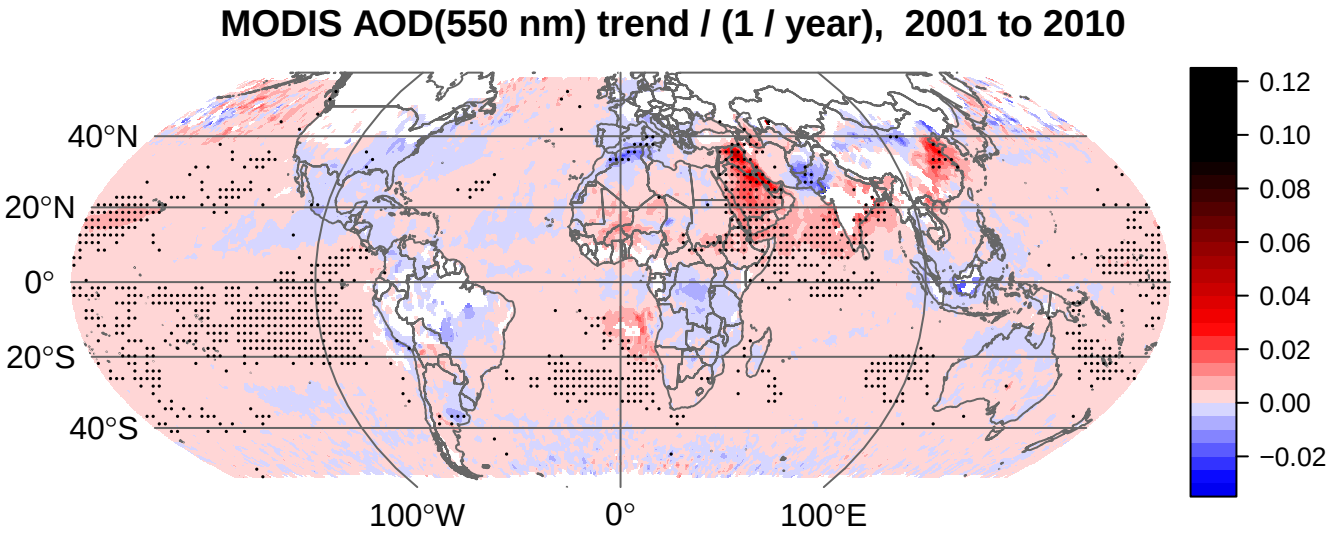

Figure S1. Same as Fig. 1 but for the ten year time period January 2001 to December 2010.

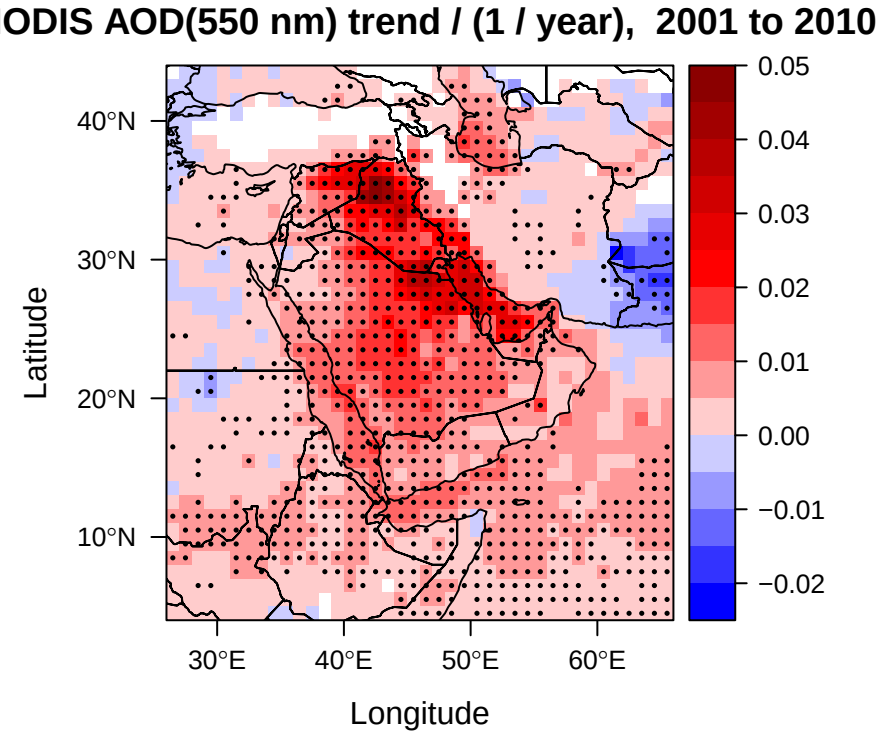

Figure S2. Same as Fig. 2 but for the ten year time period January 2001 to December 2010.

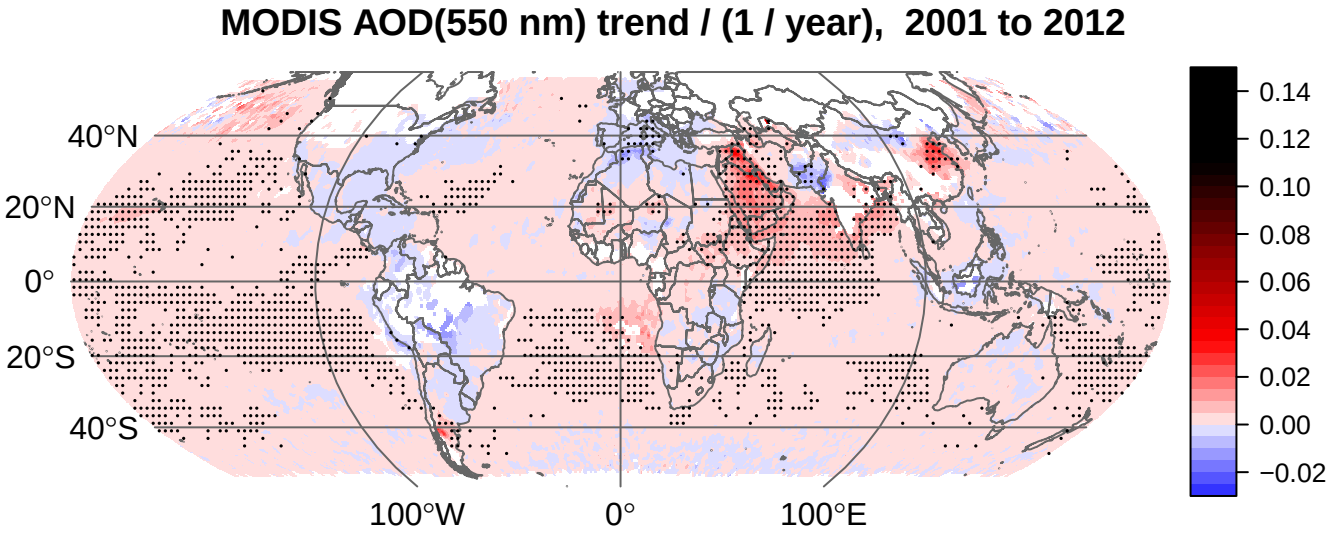

Figure S3. Same as Fig. 1 but for the twelve year time period January 2001 to December 2012.

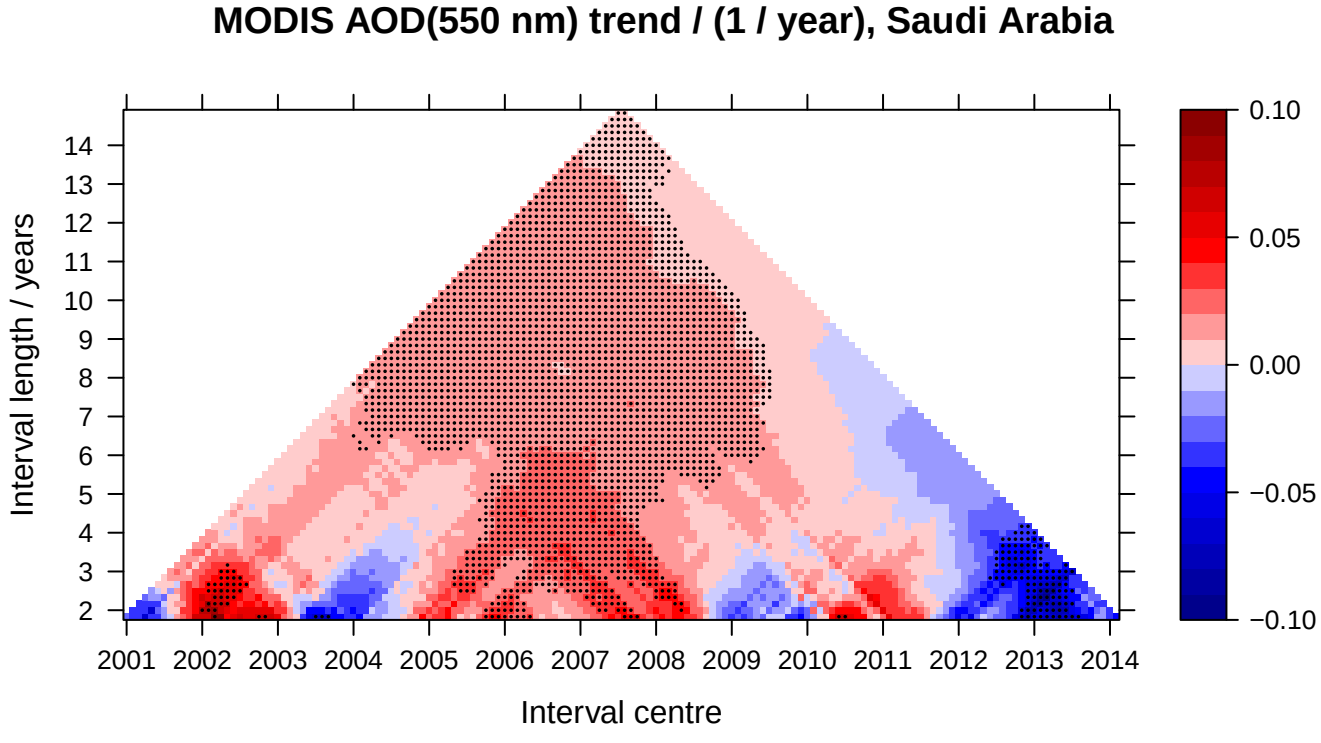

Figure S4. Trend triangle plot for the average Saudi Arabian 550 nm AOD. The abscissa depicts the centre of the time interval considered for the trend analysis using linear regression, the ordinate shows the length of the interval. Time intervals with significant trend (p value $<$ 0.01) are marked with a dot. Deseasonalisation and trend analysis is performed as for Fig. 3.

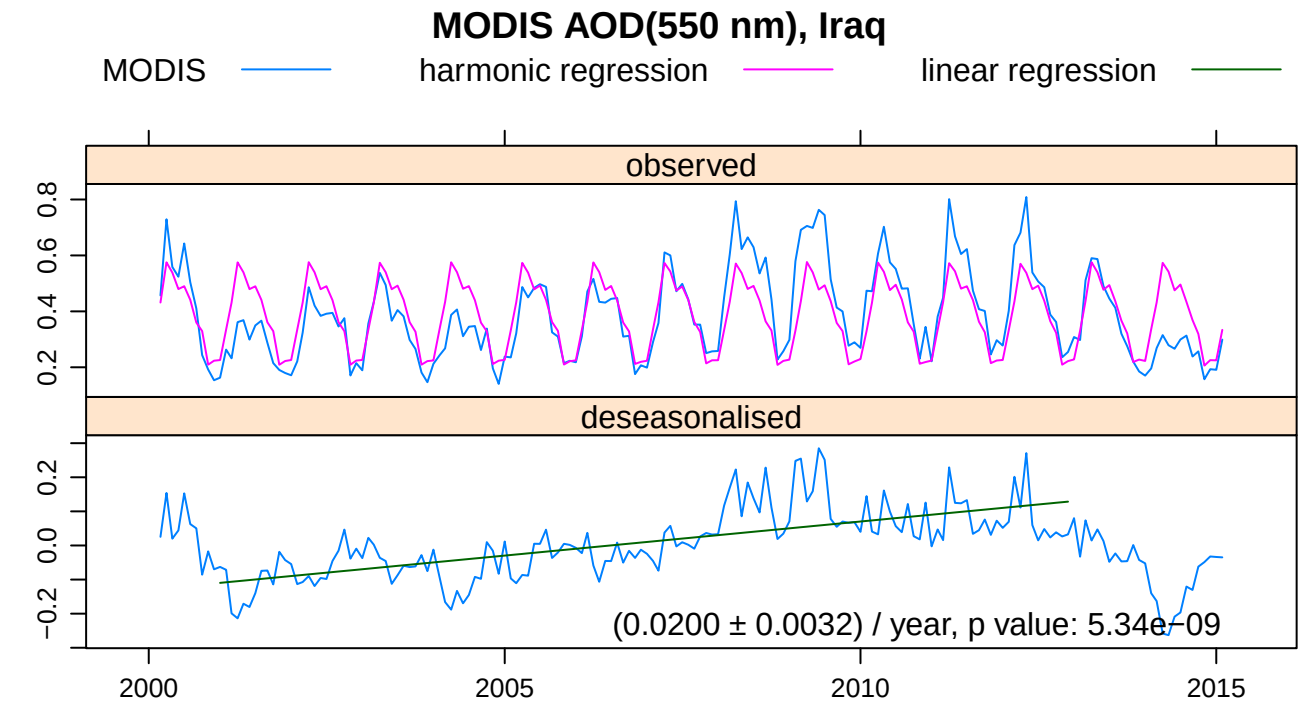

Figure S5. Same as Fig. 3, but for Iraq.

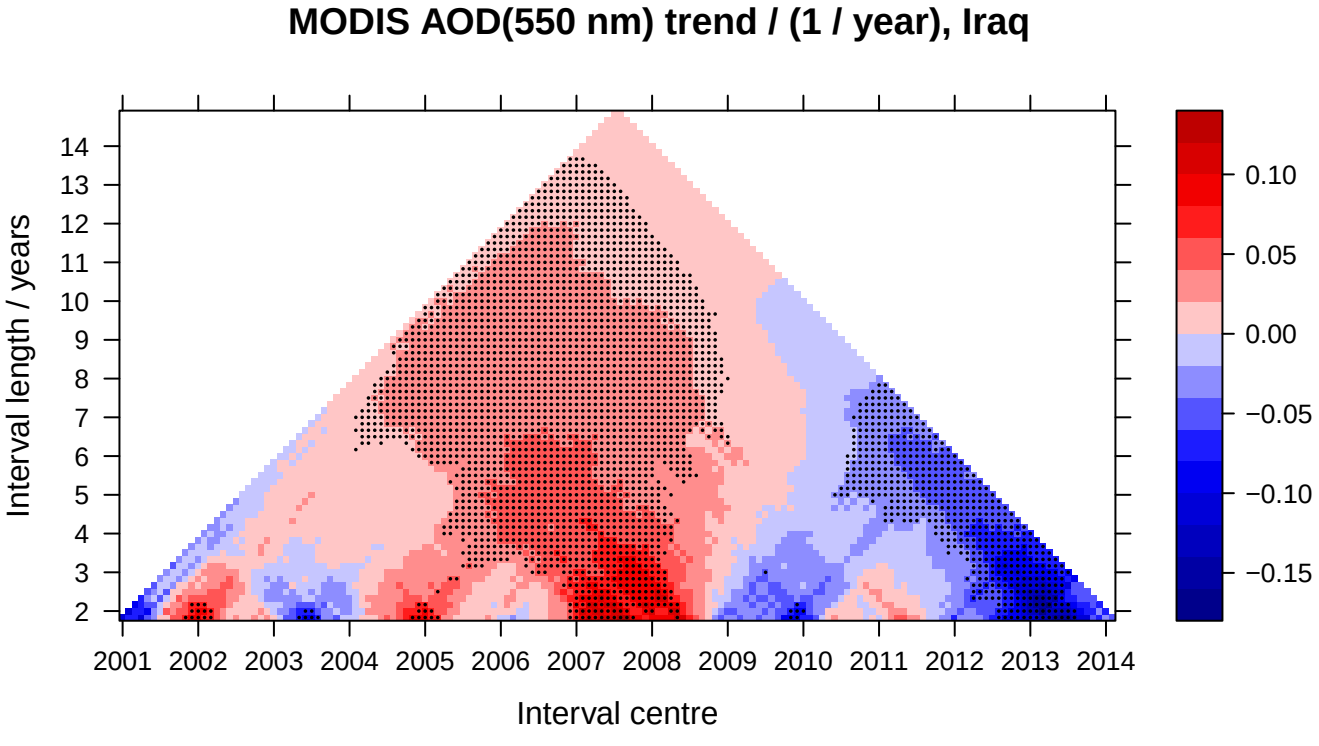

Figure S6. Same as Fig. S4, but for Iraq.

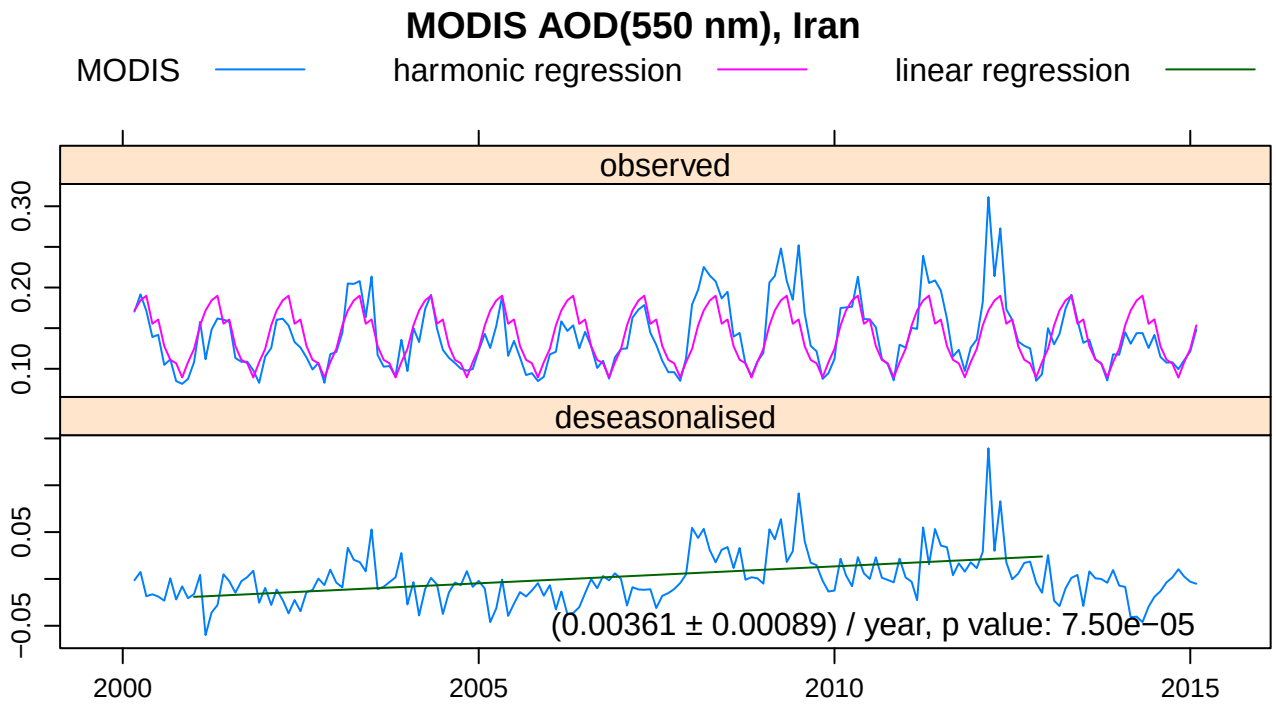

Figure S7. Same as Fig. 3, but for Iran.

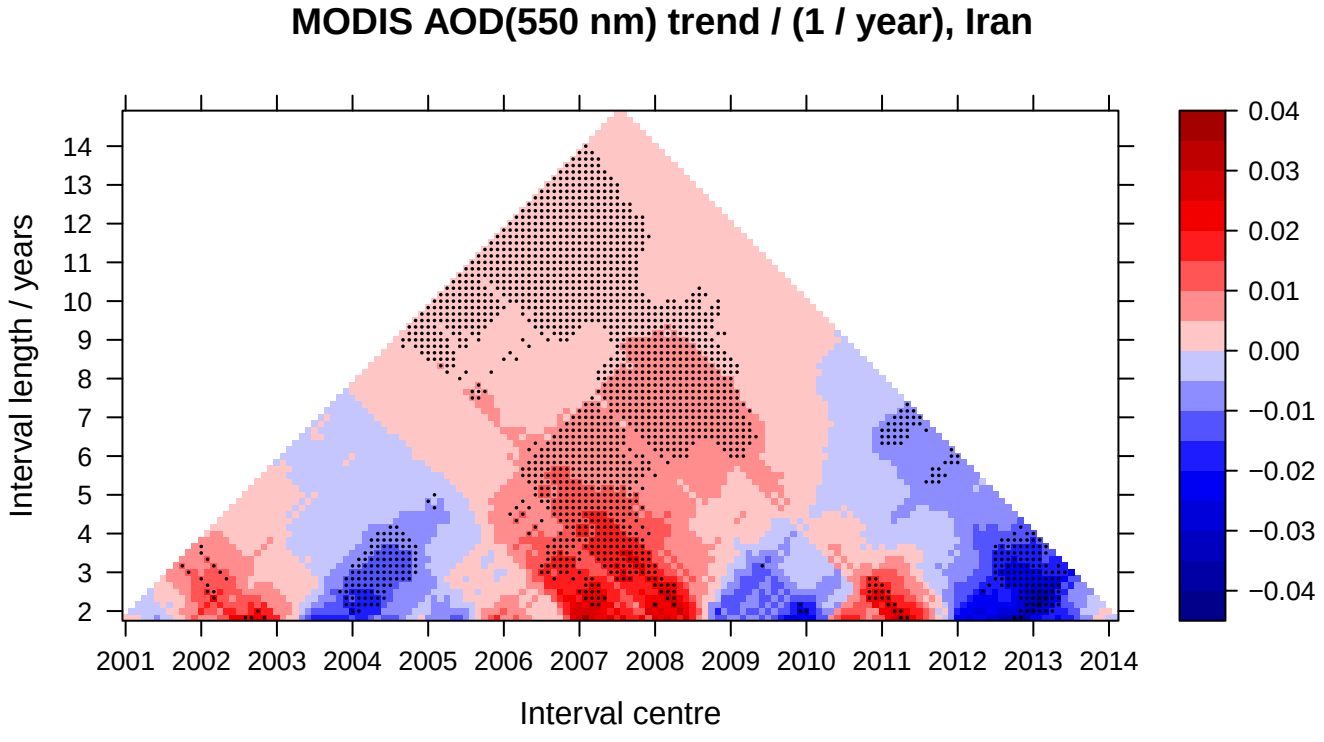

Figure S8. Same as Fig. S4, but for Iran.

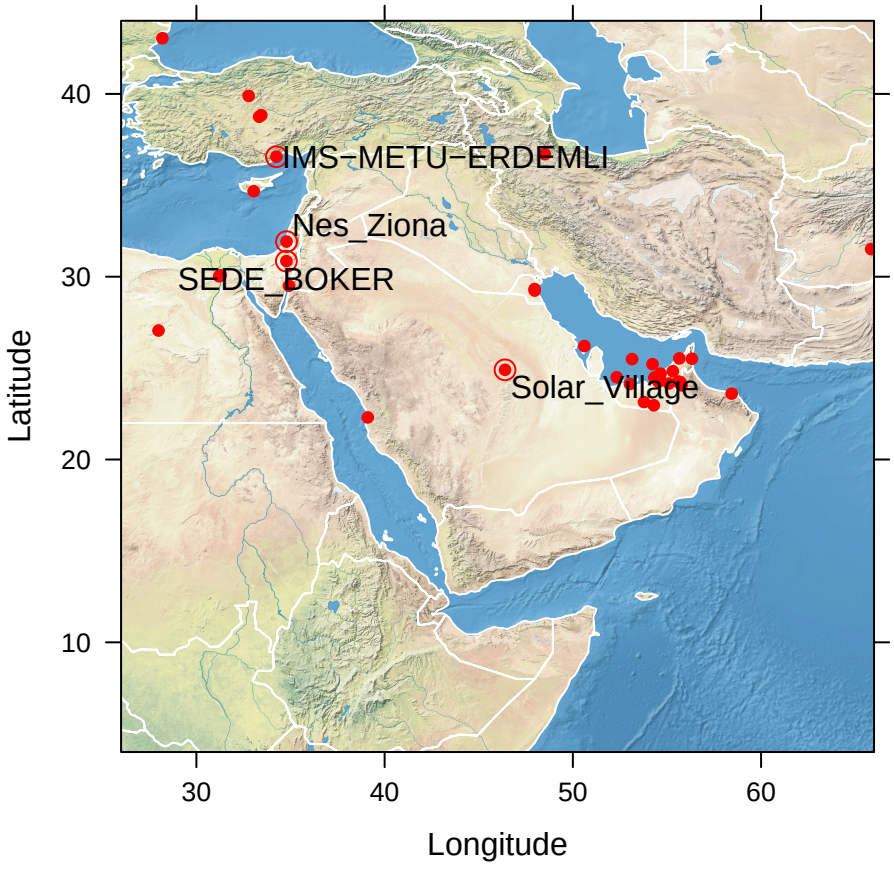

Figure S9. AERONET stations (red dots) in the region of interest. Stations with records extending over more than ten years of the current millennium are encircled and labelled.

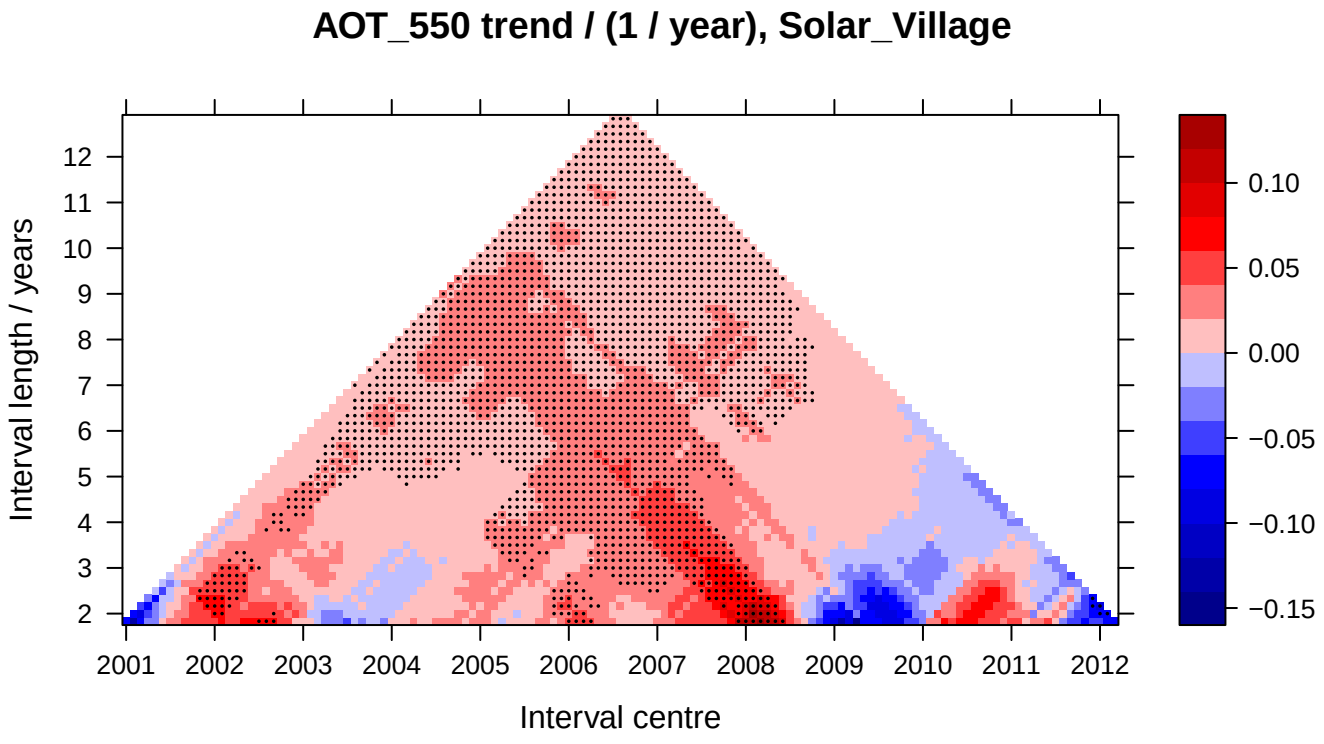

Figure S10. Same as Fig. S4, but for the AOD measured by the AERONET station *Solar Village*, linearly interpolated to 550 nm.

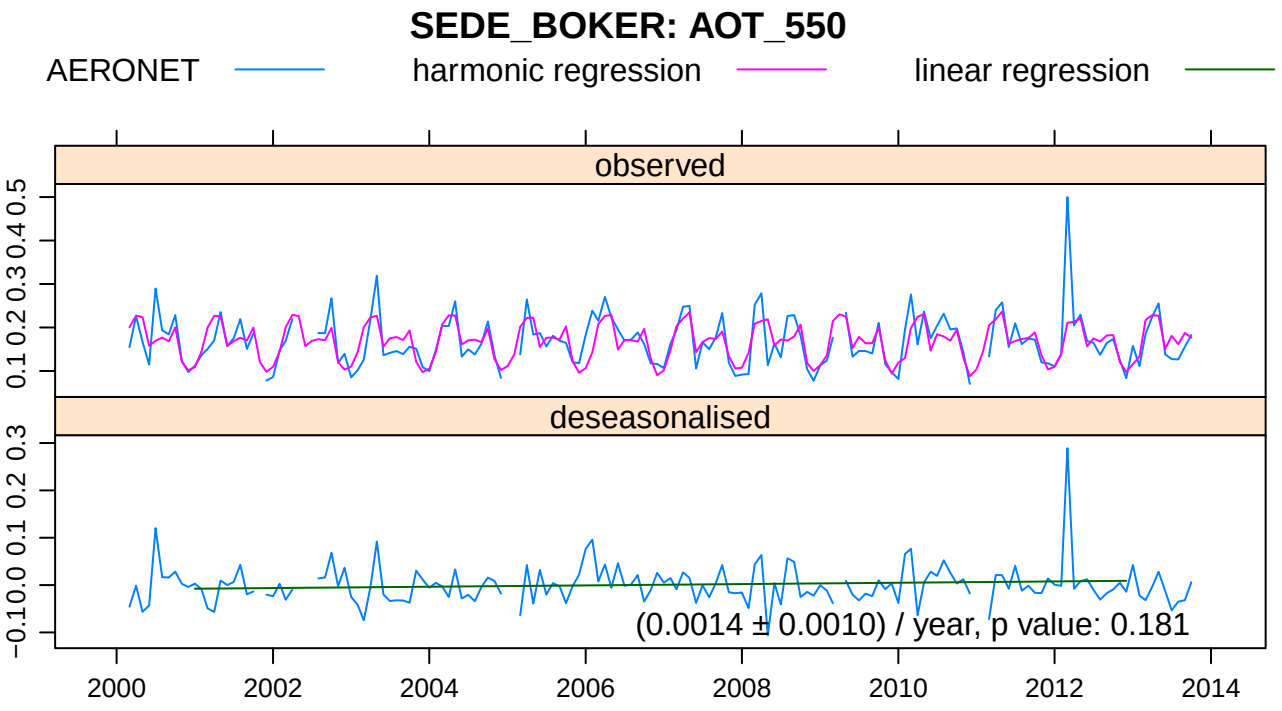

Figure S11. Same as Fig. 4, but for the AERONET station *SEDE BOKER*.

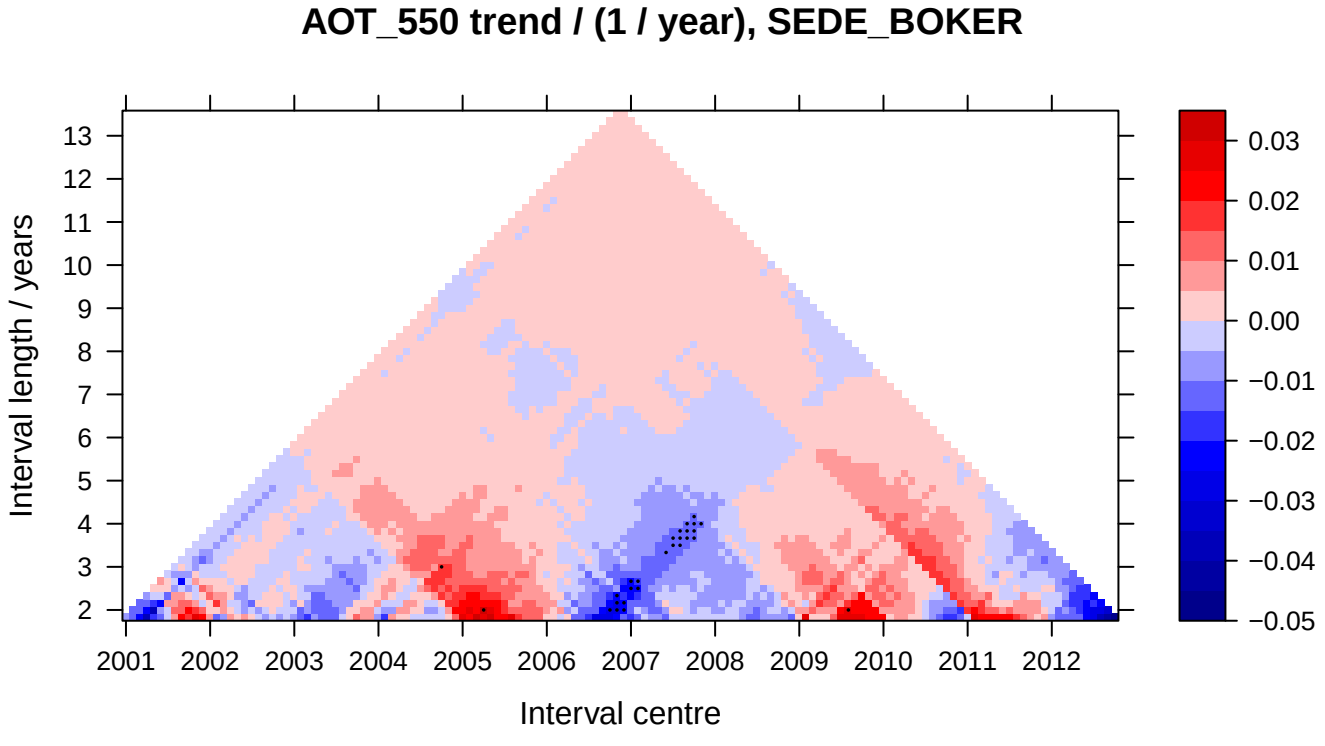

Figure S12. Same as Fig. S10, but for the AERONET station *SEDE BOKER*.

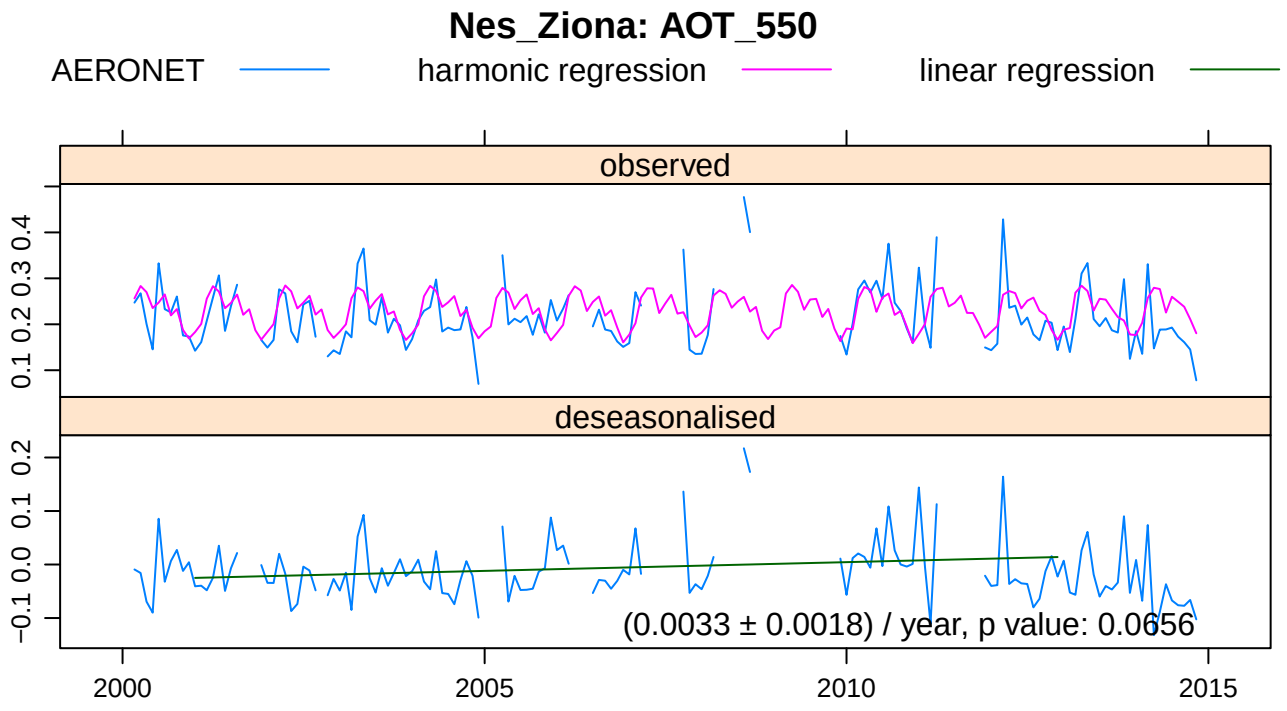

Figure S13. Same as Fig. 4, but for the AERONET station *Nes Ziona*.

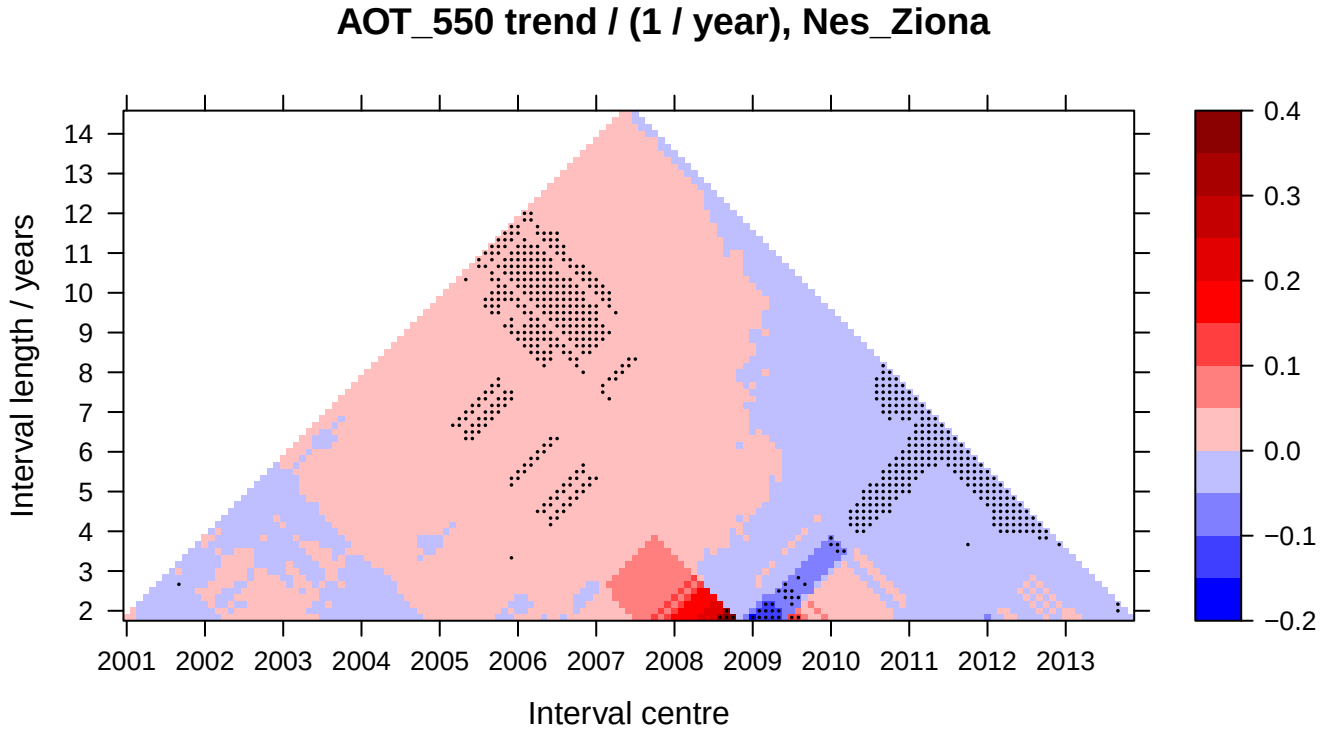

Figure S14. Same as Fig. S10, but for the AERONET station *Nes Ziona*.

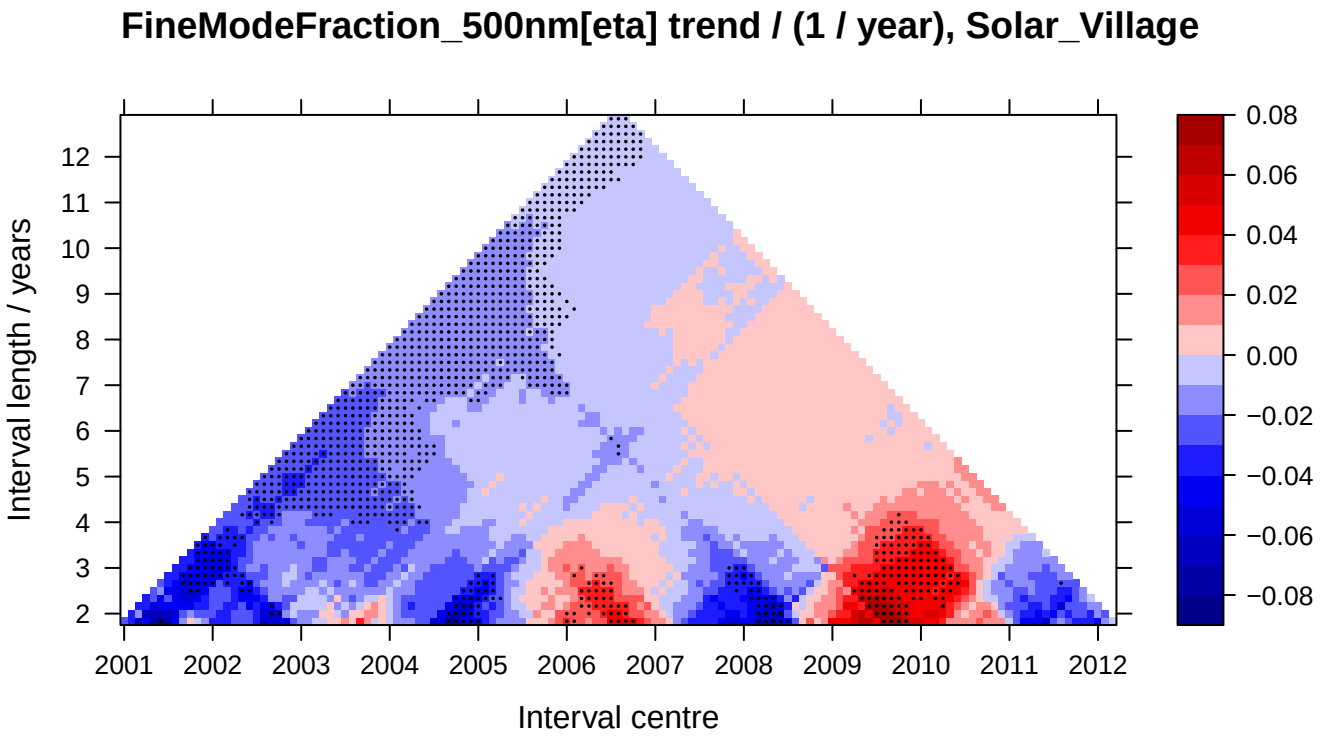

Figure S15. Same as Fig. S10 but for the AERONET fine mode fraction instead of the AOD.

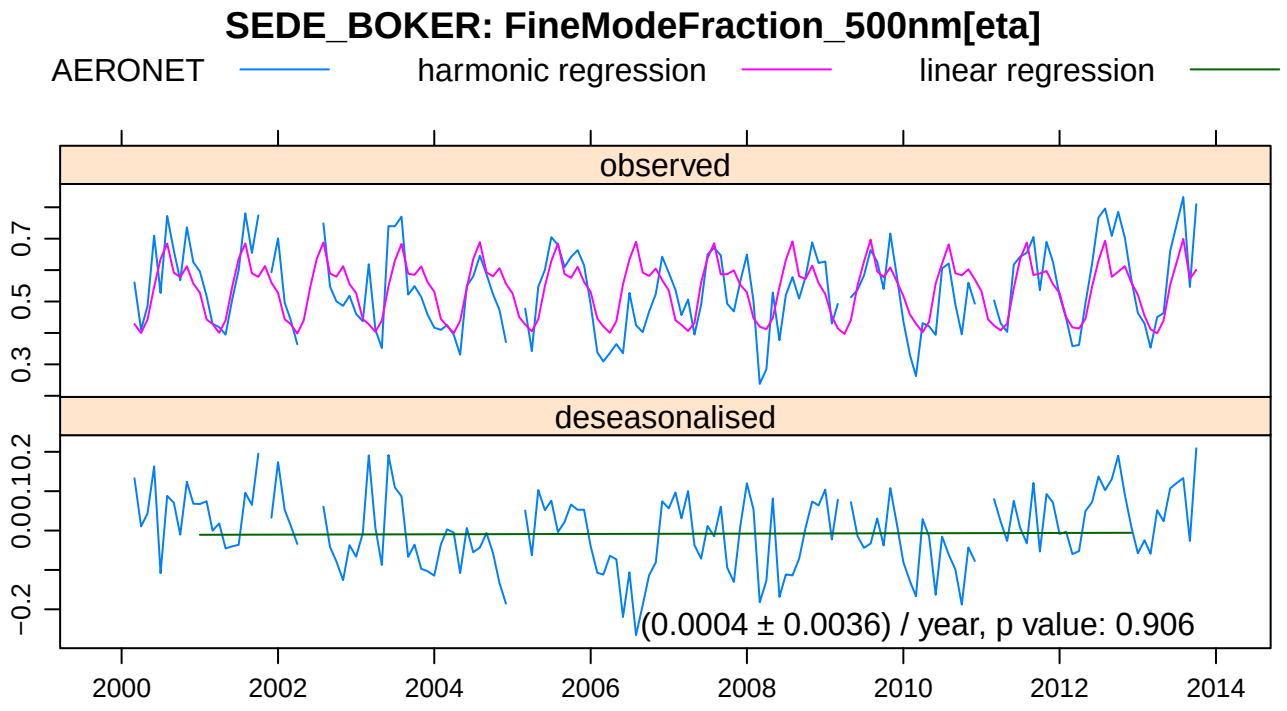

Figure S16. Same as Fig. 6 but for the AERONET station *SEDE BOKER*.

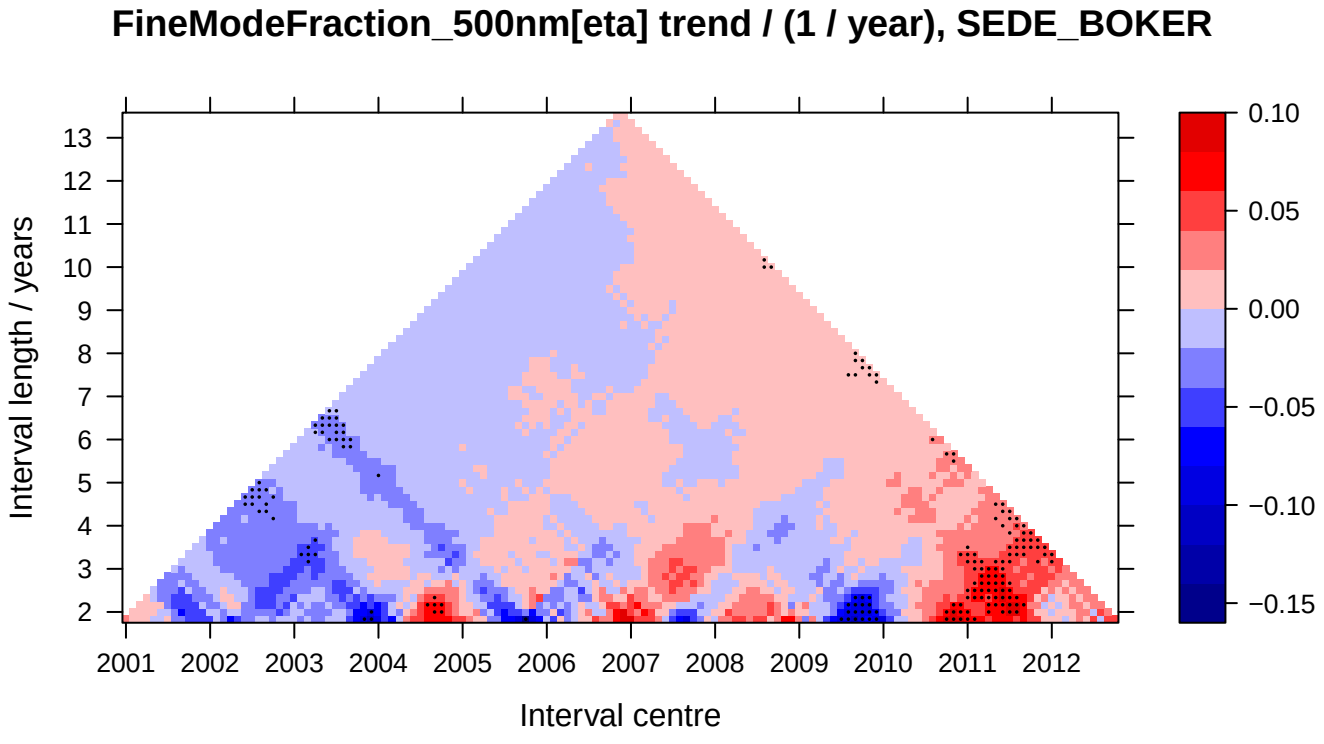

Figure S17. Same as Fig. S15 but for the AERONET station *SEDE BOKER*.

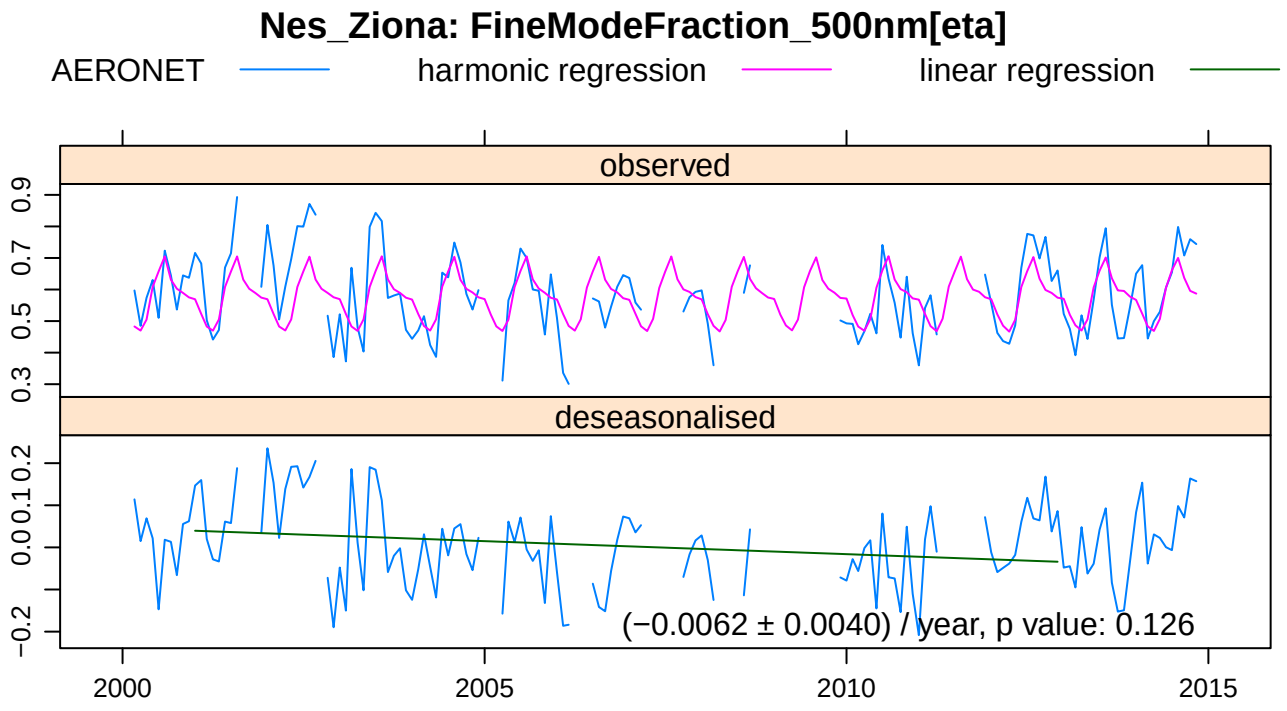

Figure S18. Same as Fig. 6 but for the AERONET station *Nes Ziona*.

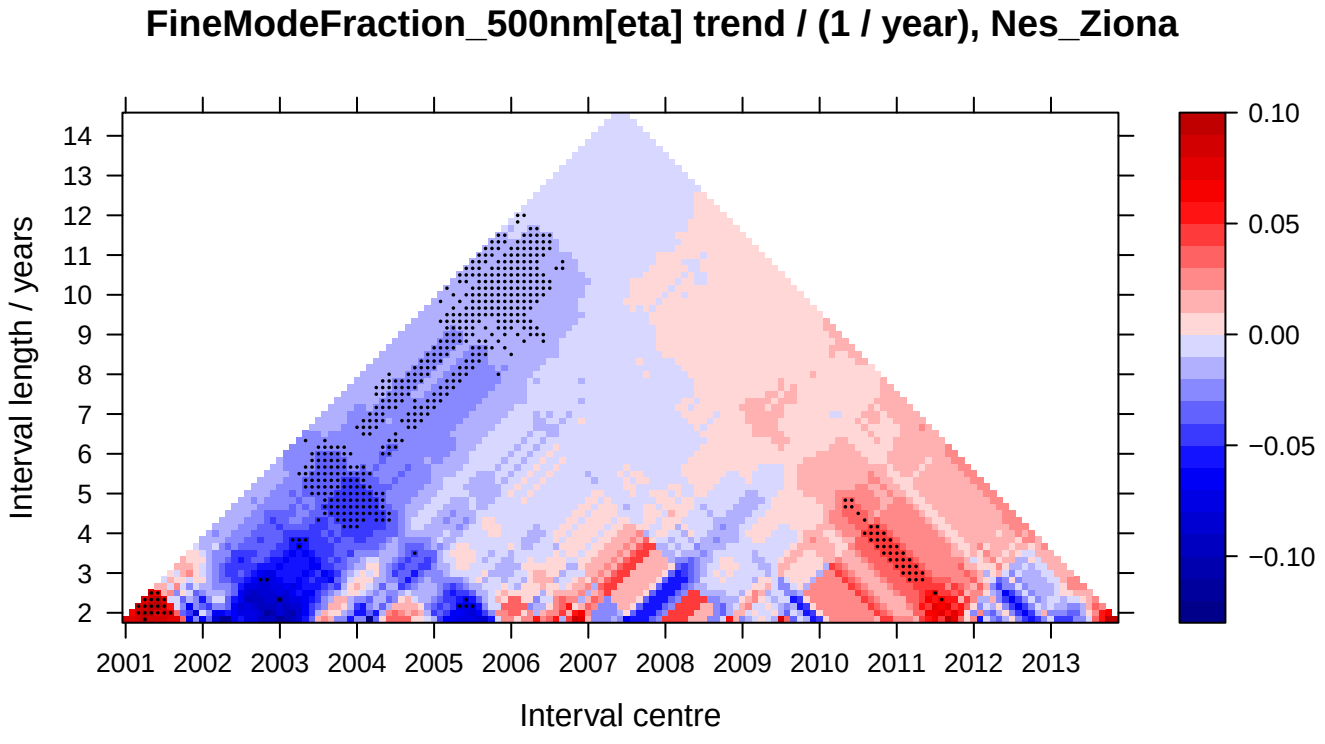

Figure S19. Same as Fig. S15 but for the station *Nes Ziona*.

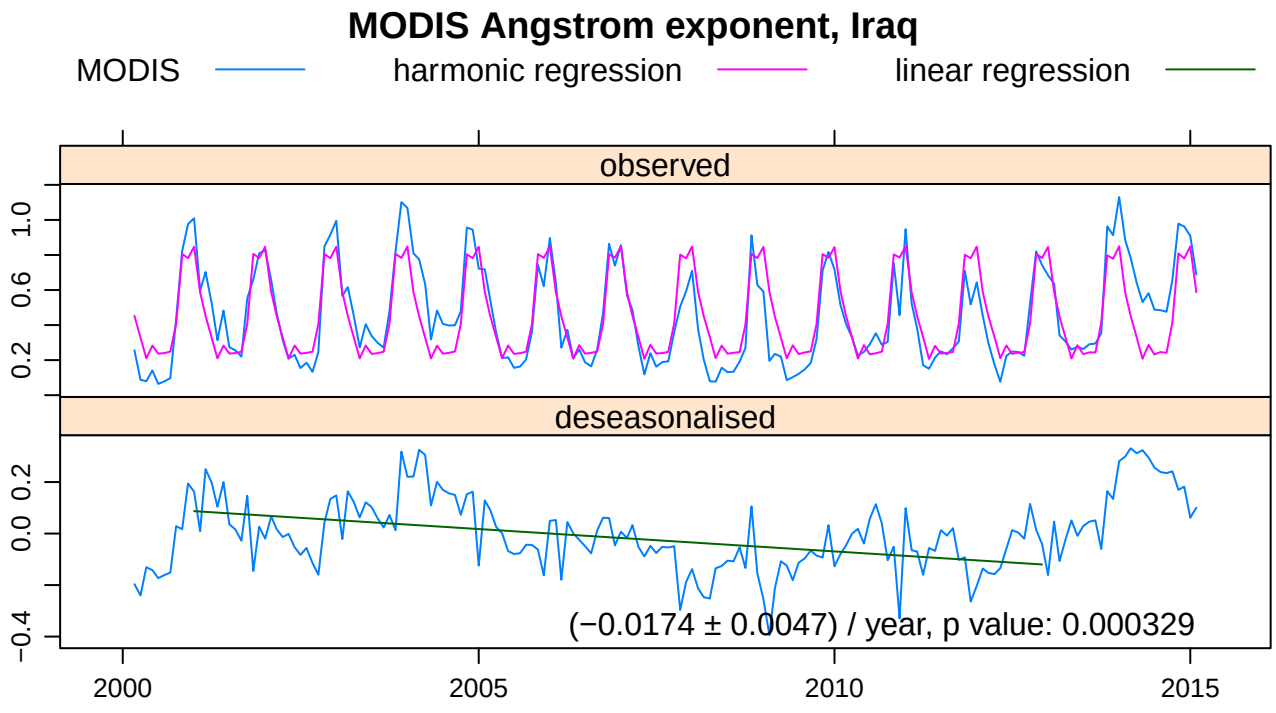

Figure S20. Same as Fig. 5, but for Iraq.

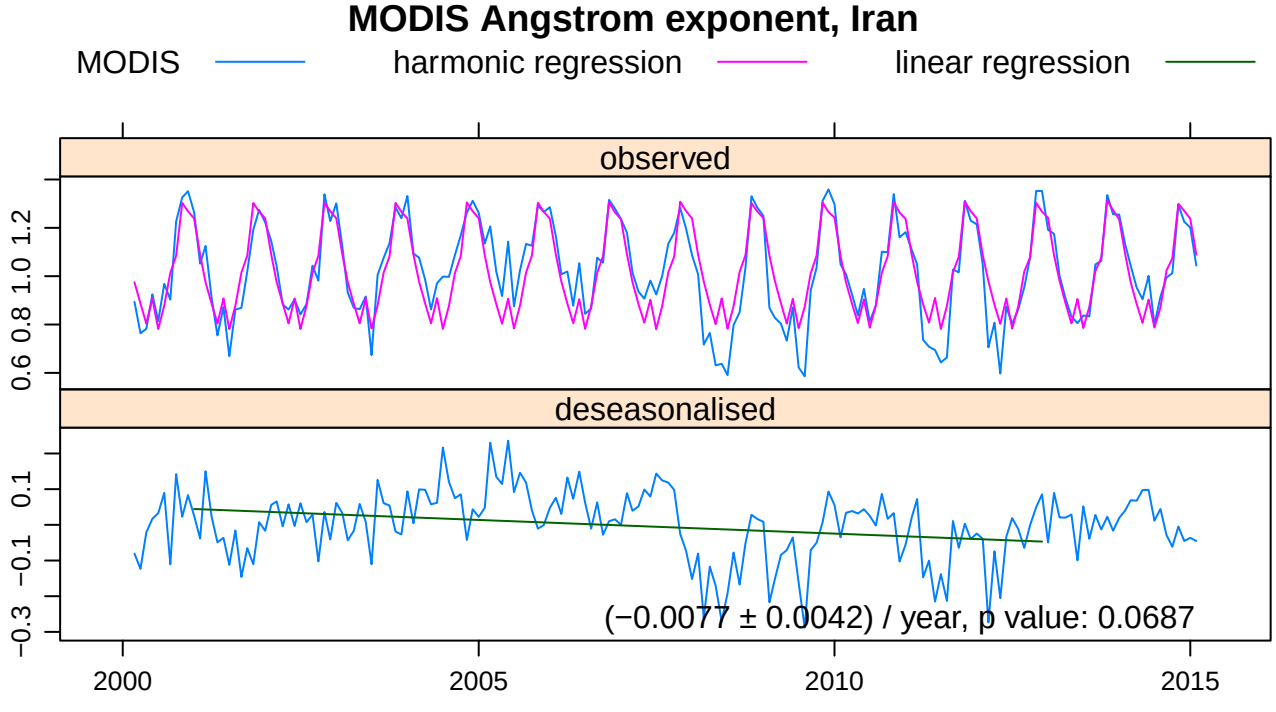

Figure S21. Same as Fig. 5, but for Iran.

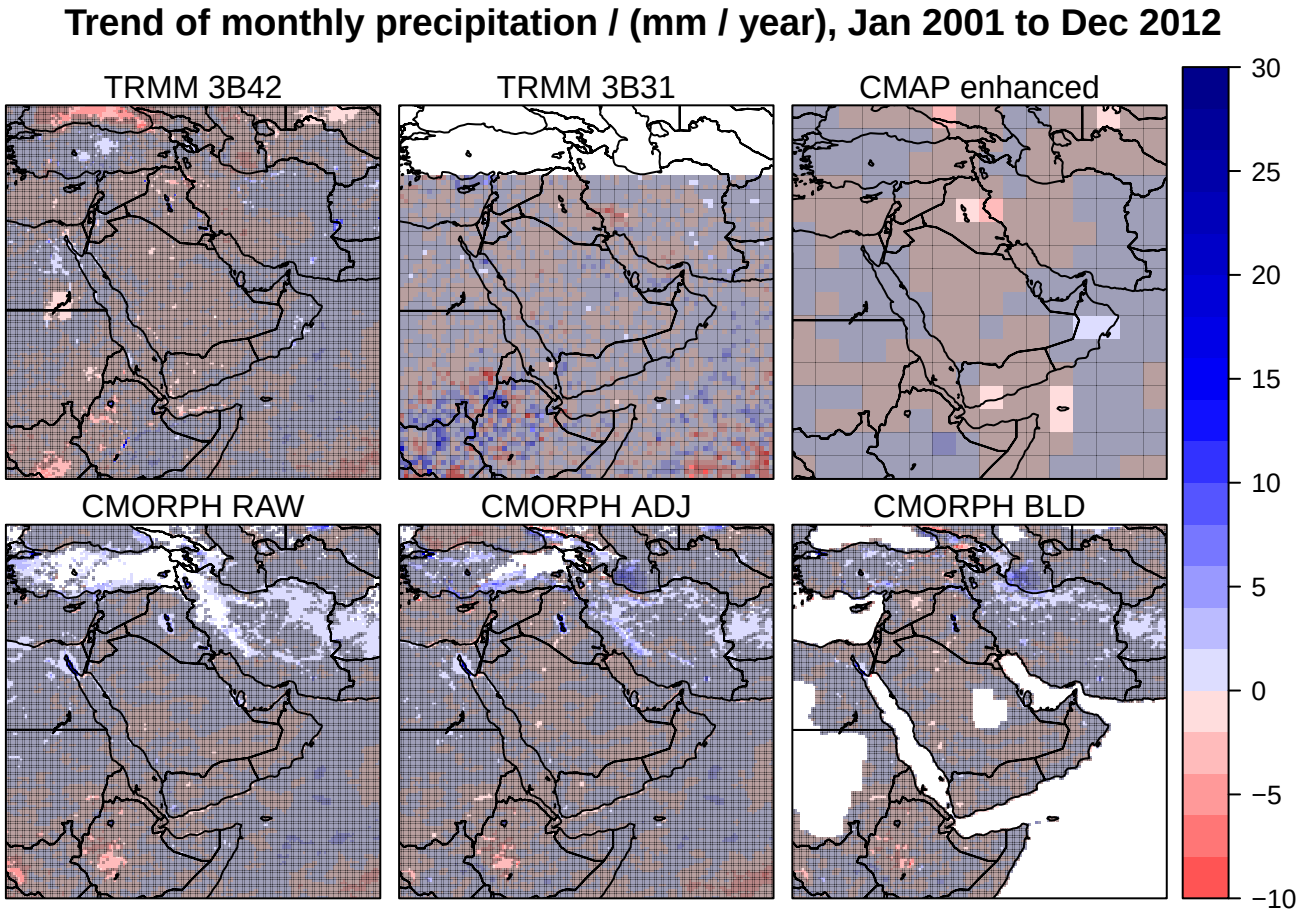

Figure S22. Pattern of Middle Eastern precipitation trends. Based on TRMM 3B42 daily, TRMM 3B31 monthly, CMAP enhanced monthly, CMORPH RAW daily, CMORPH ADJ daily and CMORPH BLD daily data, respectively. Pixels with non-significant trend (p value > 0.01) are shaded grey. See also Fig. S23.

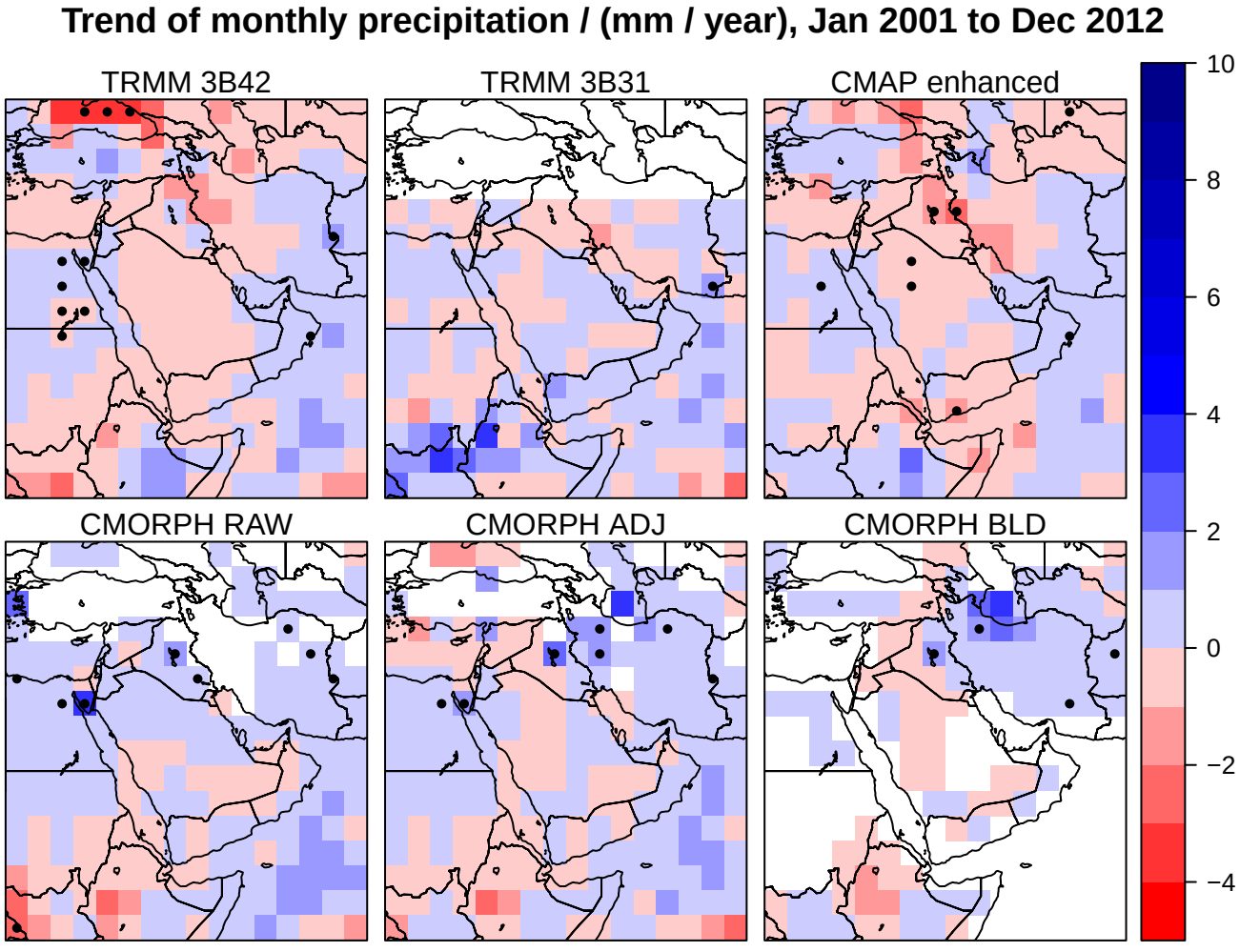

Figure S23. Pattern of Middle Eastern precipitation trends. Based on TRMM 3B42 daily, TRMM 3B31 monthly, CMAP enhanced monthly, CMORPH RAW daily, CMORPH ADJ daily and CMORPH BLD daily data, respectively. Pixels with significant trend (p value < 0.01) are marked with a dot. For better readability and to reduce statistical noise, all data sets have been re-gridded to the coarse 2.5° grid of the CMAP data (averaging over sub-pixels). Unlike for Fig. S22, annual averaged instead of deseasonalised values have been used to the compute trend, which can be more reliable in regions of very sporadic precipitation.

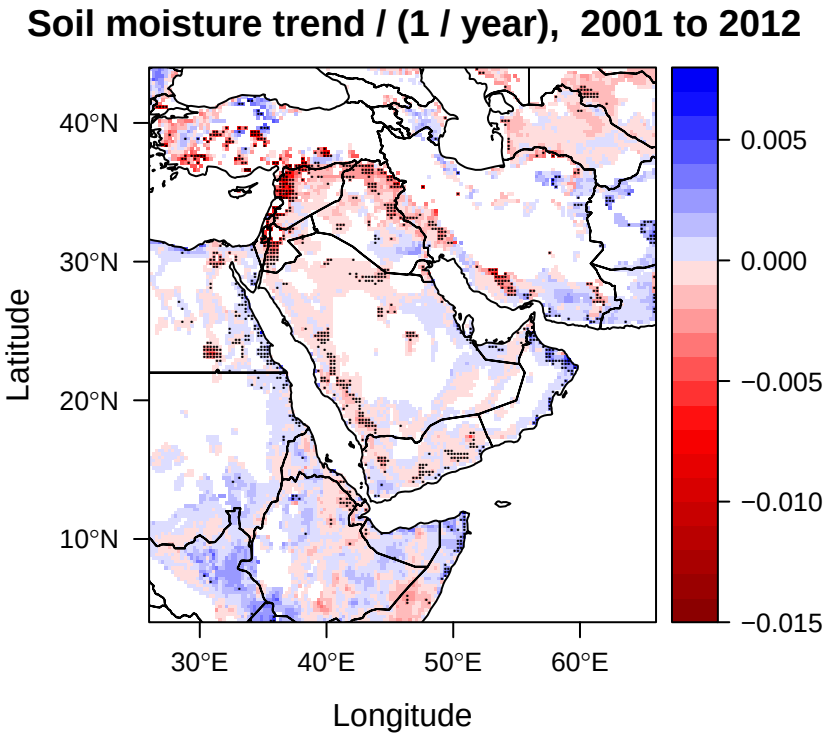

Figure S24. Pattern of Middle Eastern twelve year soil moisture trends for the twelve year period January 2001 to December 2012. Negative trends are even more pronounced when considering only the first ten years until 2010, see Fig. S25. Based on surface soil moisture (SSM) data from the European Space Agency Climate Change Initiative (ESA-CCI).

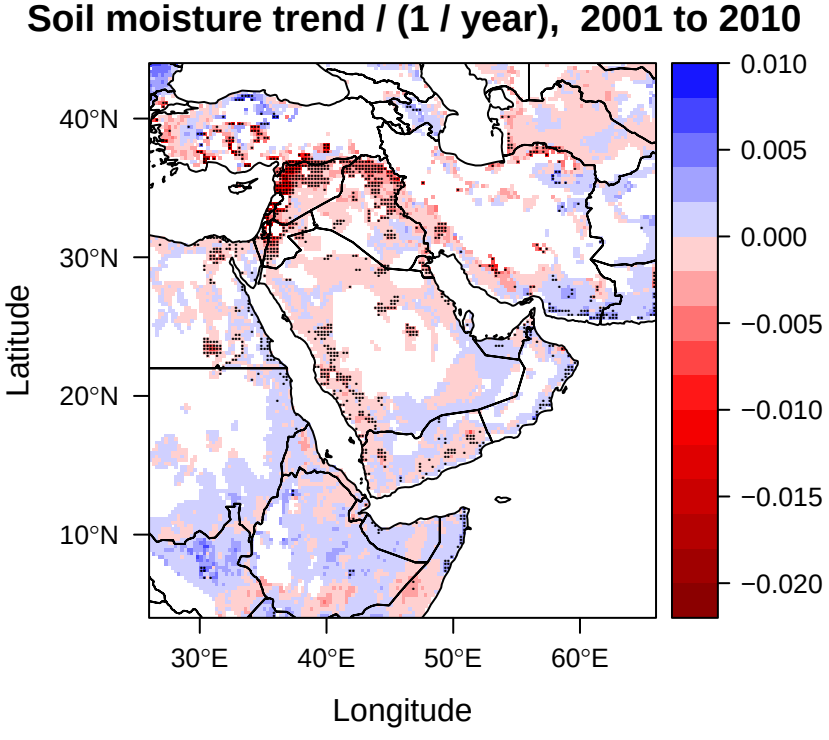

Figure S25. Same as Fig. S24 but for the time period 2001 to 2010.

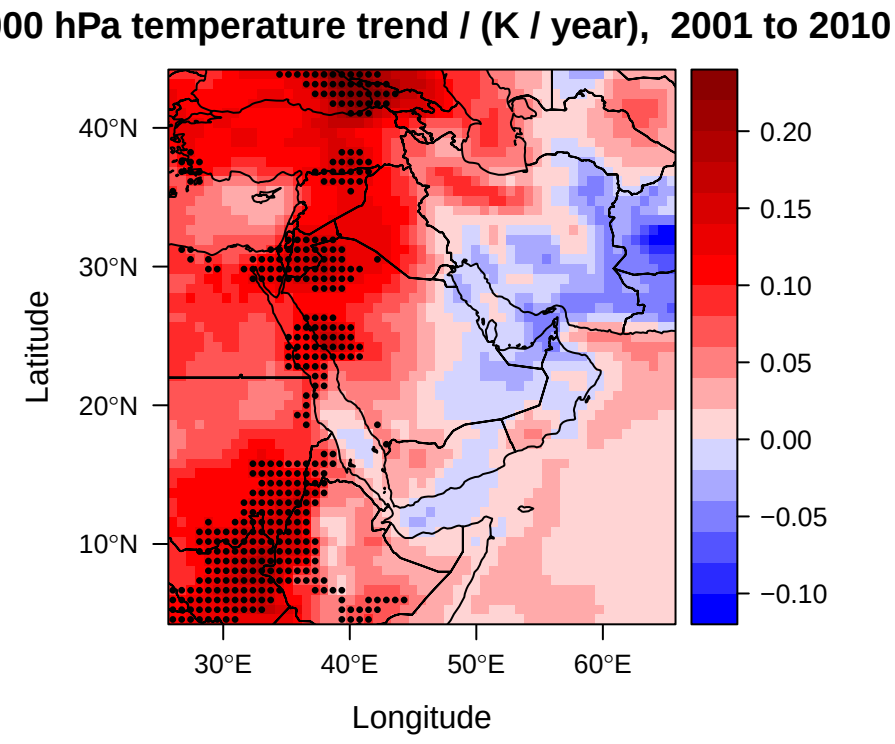

Figure S26. Pattern of Middle Eastern temperature trends (January 2001 to December 2010). The significant positive trend in several regions is interrupted by moderate temperatures in 2011, possibly slowing down the negative soil moisture trend (cp. S24 vs. S25). Based on the ERA-Interim 1000 hPa temperature.

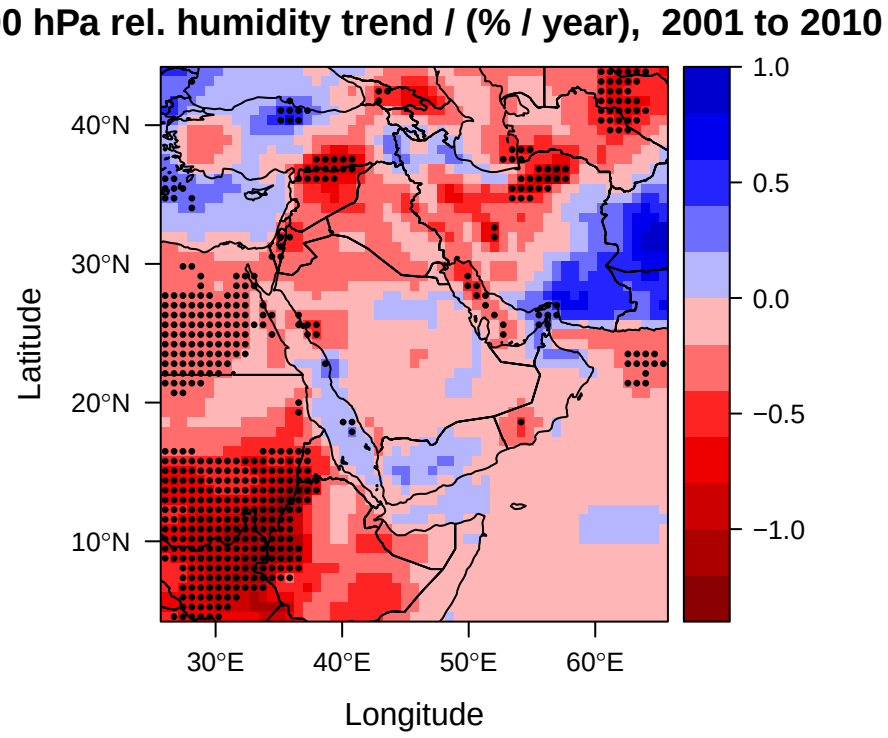

Figure S27. Pattern of Middle Eastern relative humidity trends (January 2001 to December 2010). Based on the ERA-Interim 1000 hPa relative humidity.

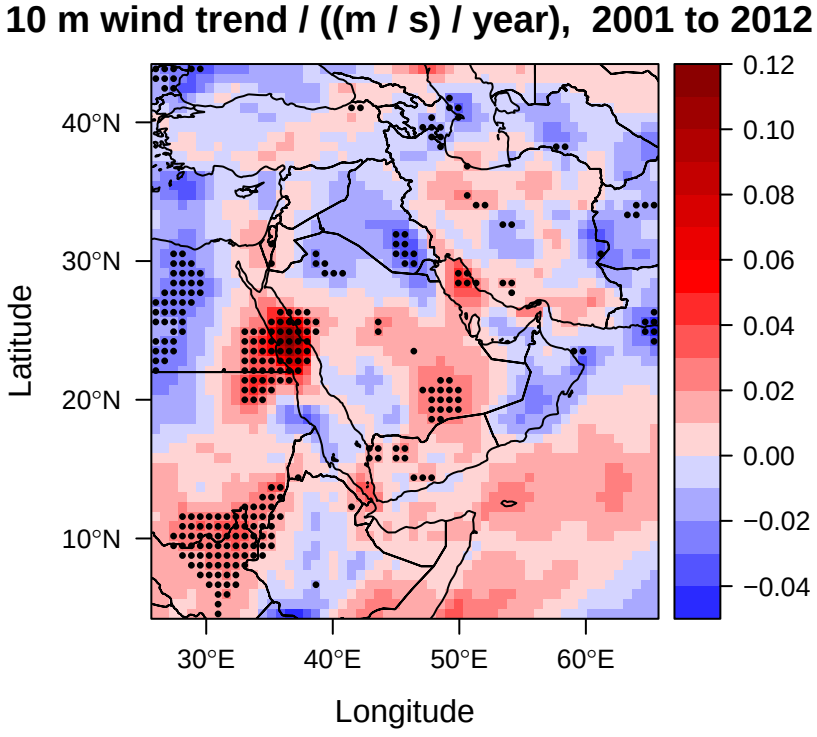

Figure S28. Pattern of Middle Eastern surface wind trends. Based on ERA-Interim wind at 10 m altitude.

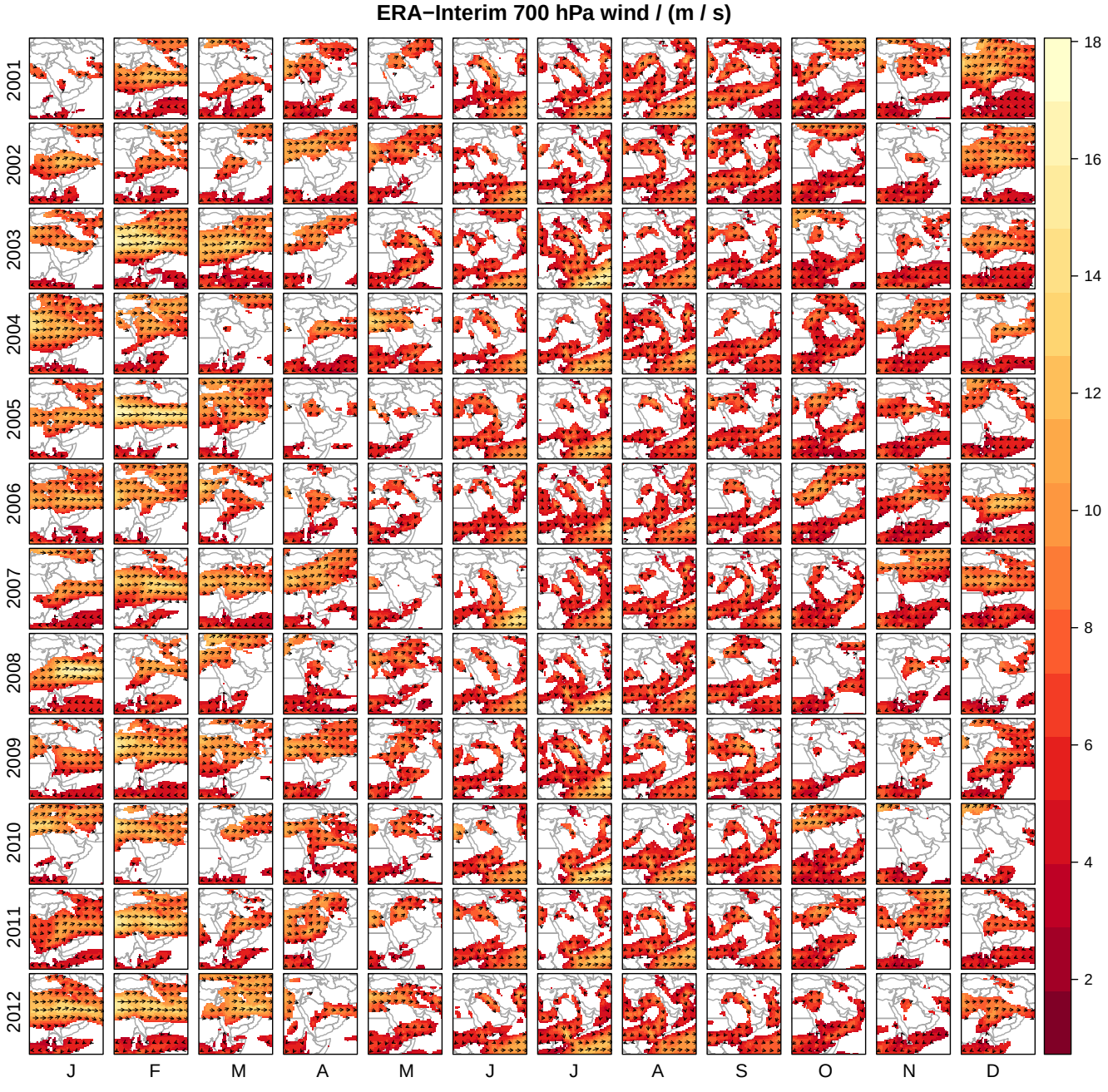

Figure S29. ERA-Interim wind at 700 hPa. To expose persistent transport patterns, monthly average wind vectors $(\bar{u}, \bar{v})^T$ are plotted if their magnitude exceeds $\sqrt{\sigma(u)^2 + \sigma(v)^2}$, where σ denotes the standard deviation of the six-hourly values. The colour scale reflects the vector magnitude.

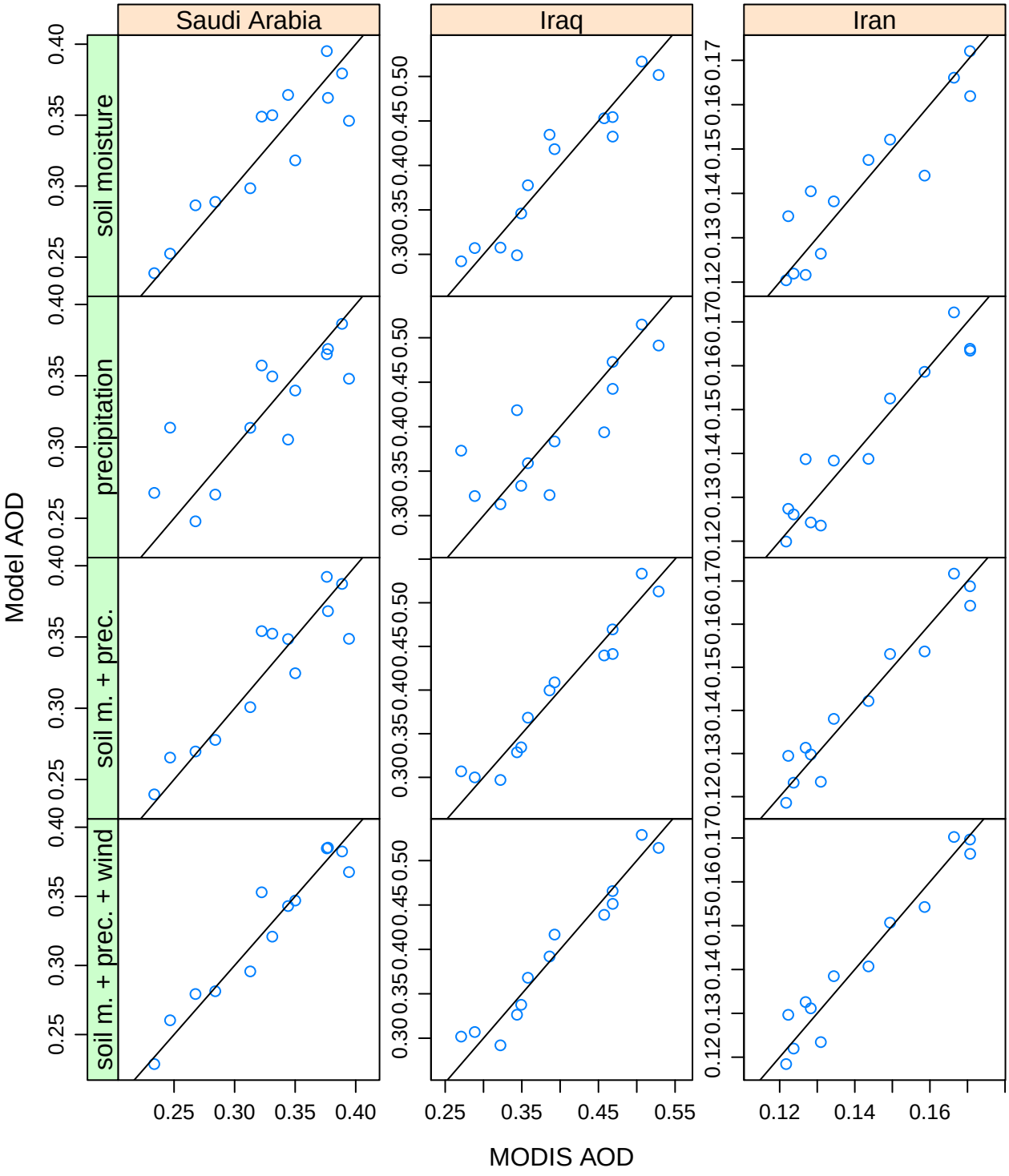

Figure S30. Linear model vs. MODIS AOD for the models in Tab. 1. The model predictors used in each row are displayed in the strip on the left. For Iraq and Iran, good model results are obtained when using soil moisture and precipitation as predictors (third row). For Saudi Arabia, the model can be improved by additionally considering the surface wind (bottom left).

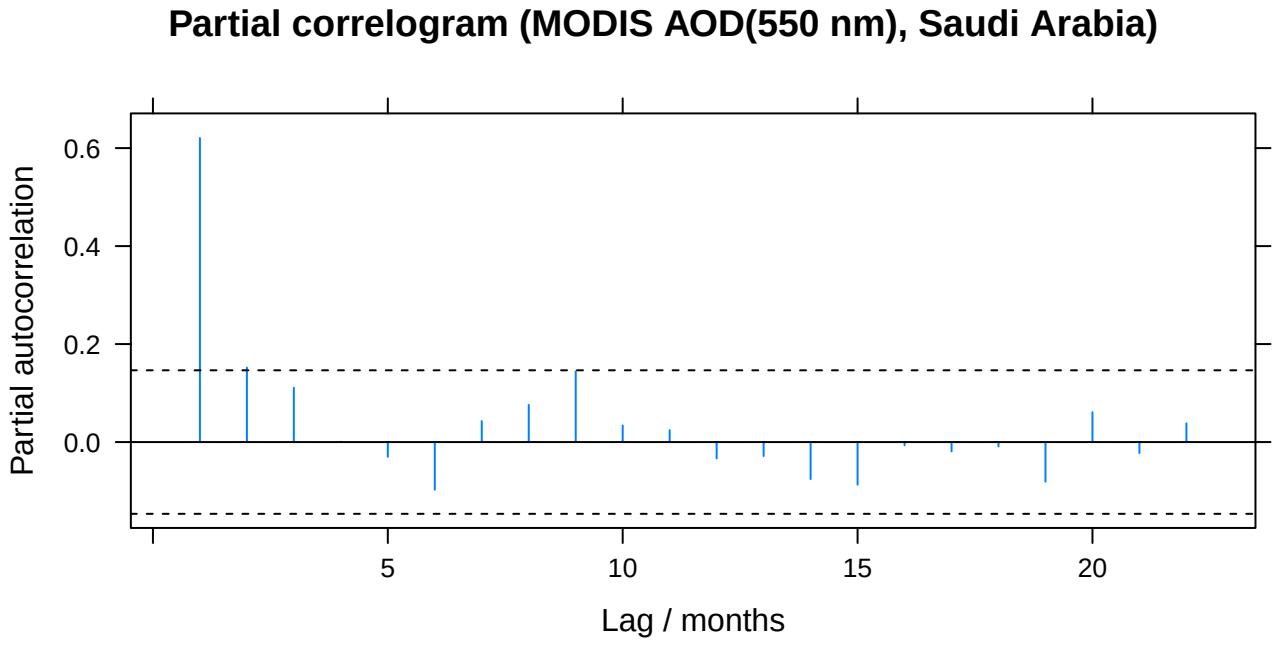

Figure S31. Partial correlogram of the deseasonalised MODIS AOD time series over Saudi Arabia in Fig. 3. The dashed lines represent the confidence limits for a significance level of 5%. Only the 1 month lag partial autocorrelation is unambiguosly significant, suggesting that the time series follows an AR(1) process. The absence of a significant partial autocorrelation for a 12 month lag demonstrates the good performance of the deseasonalisation procedure.

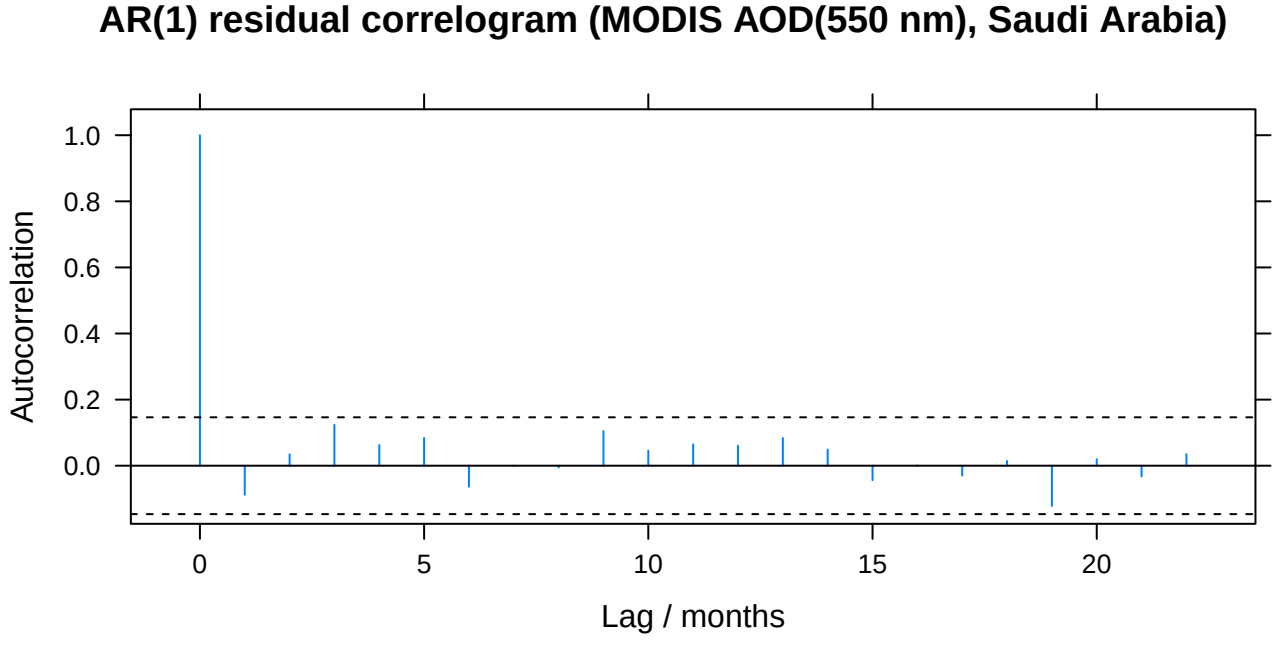

Figure S32. Correlogram for the residuals of the AR(1) model fitted to the deseasonalised MODIS AOD time series over Saudi Arabia in Fig. 3. The dashed lines represent the confidence limits for a significance level of 5%. No significant autocorrelations are found, providing evidence that the residuals are well approximated by white noise and that the AR(1) model yields a good approximation of the deseasonalised time series.

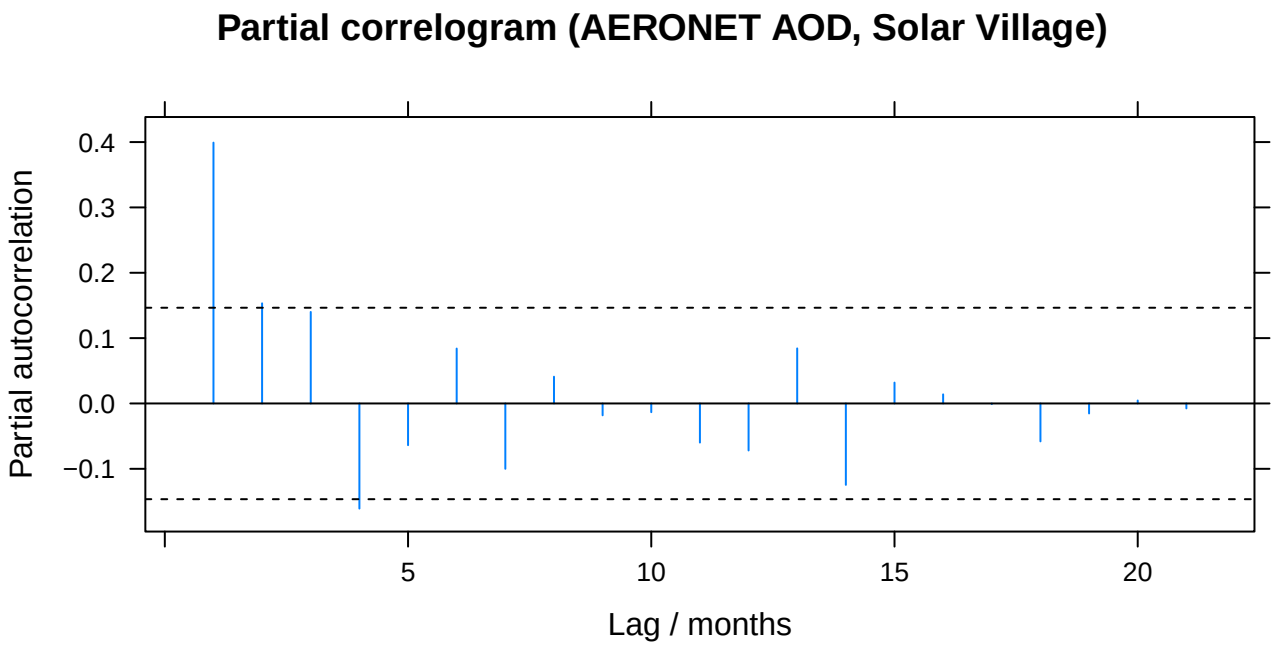

Figure S33. As Fig. S31, but for the AERONET AOD over Solar Village shown in Fig. 4.

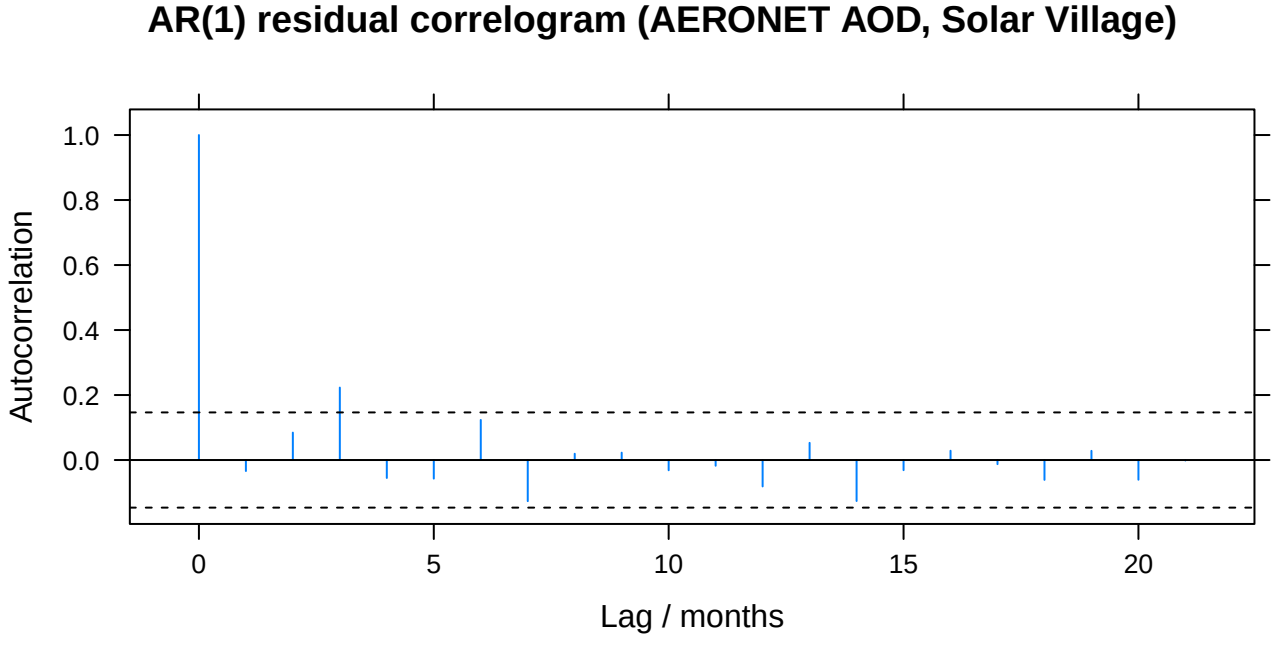

Figure S34. As Fig. S32, but for the AERONET AOD over Solar Village shown in Fig. 4.

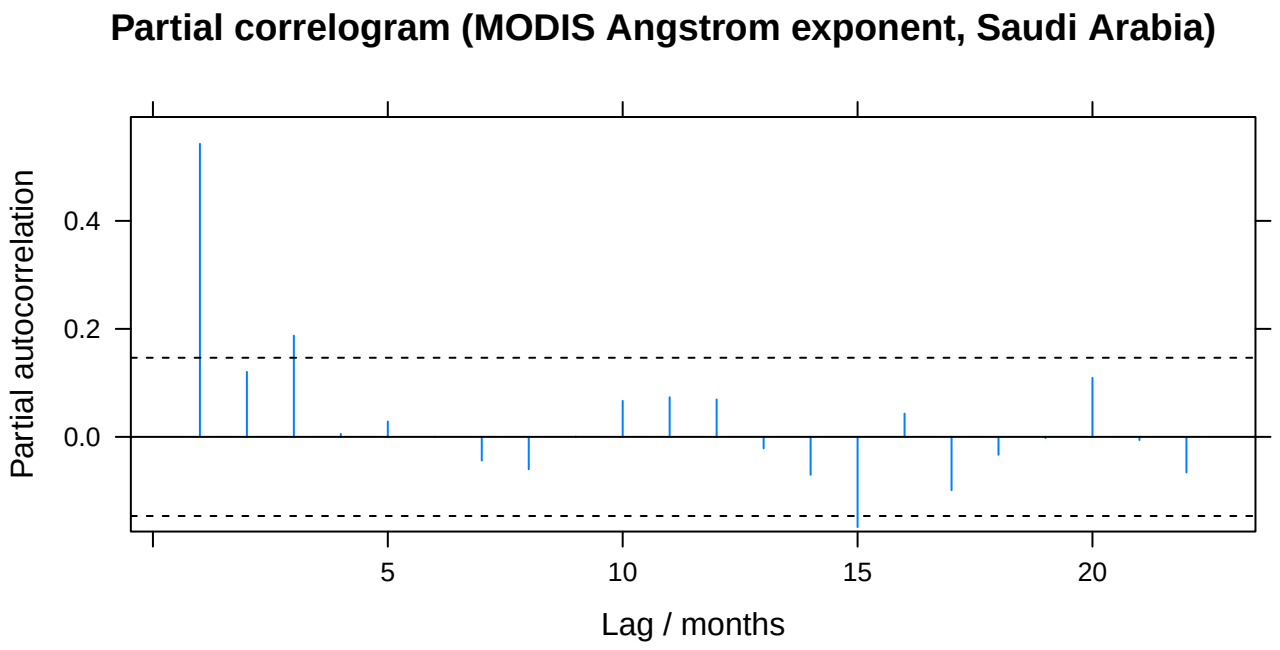

Figure S35. As Fig. S31, but for the MODIS Ångström exponent shown in Fig. 5.

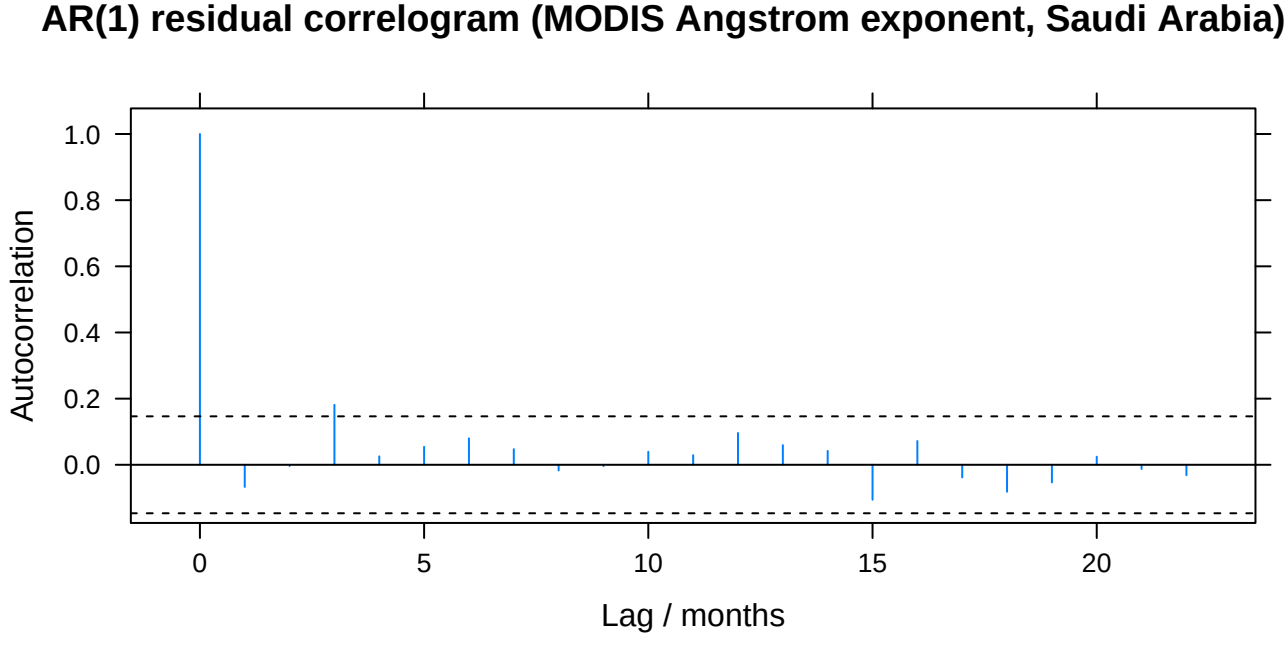

Figure S36. As Fig. S32, but for the MODIS Ångström exponent shown in Fig. 5.

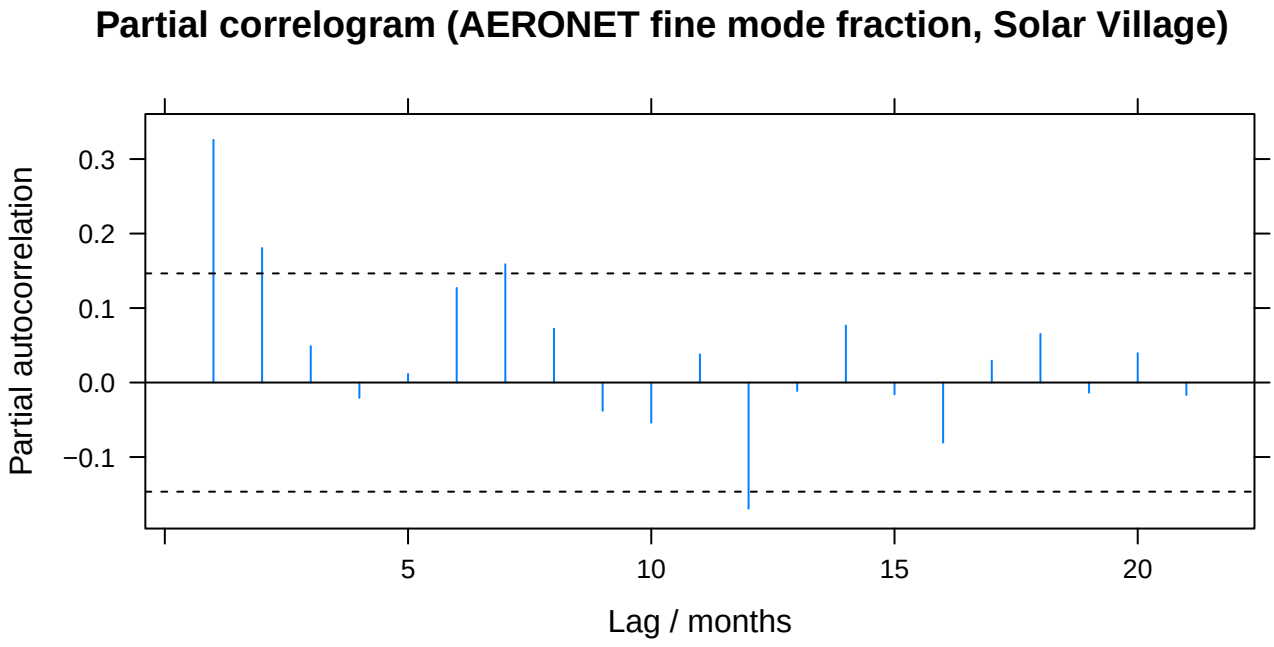

Figure S37. As Fig. S31, but for the AERONET fine mode fraction over Solar Village shown in Fig. 6.

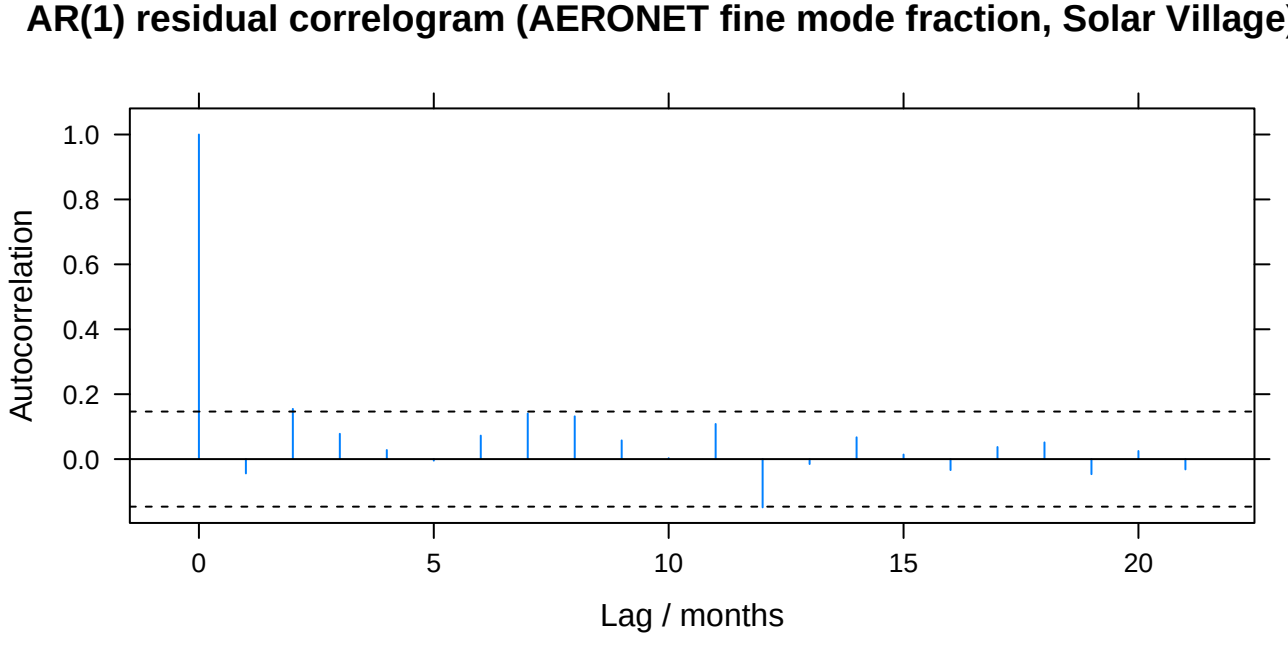

Figure S38. As Fig. S32, but for the AERONET fine mode fraction over Solar Village shown in Fig. 6.

Aral Sea AOD trends

Our analysis identifies the strongest trend in the monthly level 3 MODIS AOD product (MODIS MOD08 M3) over the Aral Sea region. The dust activity in this region is increasing due to the drying Aral Sea which exposes new dust sources (Wiggs et al., 2003). However, due to rapidly changing shorelines and land cover, and the lack of ground based observations for validation, space-borne AOD retrievals over this region are very challenging (Sayer, 2016). This suggests that the extreme MODIS trend is not real in its full magnitude, but includes a spurious component due to retrieval artefacts, and motivates a more detailed analysis of the AOD data in question.

Figure Fig. S39 shows the time series of the one degree cell with the centre 44.5°N59.5°W in the Aral Sea region, which corresponds to the maximum in Fig. 1. The data exhibits a very constant growth over the 15 year period, i.e., the trend does not result from a few years of high AOD, and the small p value indicates a very high significance of the trend. What often characterises a reliable result for an AOD trend, in view of the shrinking Aral Sea rather appears to be a spurious drift related to the changing surface reflectance, in particular due to the changing shorelines. This is further supported by the extremely high AOD values towards the end of the period which suggest that the surface in reality is brighter than assumed for the retrieval algorithm.

Figure S40 shows that the high AOD values and the strong positive trend is restricted to only a few grid cells. The same cells suffer from a low number of AOD retrievals per month (Fig. S41), revealing difficult retrieval conditions. Moreover, in their AOD histograms, Fig. S42, the bin for large AOD values above 1.5 has a frequency comparable to that of bins for lower AOD values which under normal conditions does not occur. Based on this observation, a simple filter can be used to filter out the affected grid cells in the Aral Sea region with little impact on the retrievals globally: for considering a grid cell the frequency of the bin for large AODs (1.5 to 5) is required to be smaller than the mean frequency of all bins (0 to 0.1, 0.1 to 0.3, 0.3 to 0.6, 0.6 to 1.5, 1.5 to 5). As Fig. S43 shows, this condition is fulfilled almost globally. Applying the filter to Fig. 1 yields Fig. S44, where the AOD trend has an upper limit of about 0.025 per year.

References

Klingmüller, K., Pozzer, A., Metzger, S., Stenchikov, G., and Lelieveld, J.: Aerosol optical depth trend over the Middle East, Atmospheric Chemistry and Physics Discussions, 2016, 1–30, doi:10.5194/acp-2015-839, http://www.atmos-chem-phys-discuss.net/acp-2015-839/, 2016.

MODIS MOD08 M3: ftp://ladsweb.nascom.nasa.gov/allData/6/MOD08_M3/, visited 31 Aug 2015.

Sayer, A. M.: personal communication, see also online discussion of Klingmüller et al. (2016), 2016.

Wiggs, G. F. S., O'hara, S. L., Wegerdt, J., Van Der Meer, J., Small, I., and Hubbard, R.: The dynamics and characteristics of aeolian dust in dryland Central Asia: possible impacts on human exposure and respiratory health in the Aral Sea basin, Geographical Journal, 169, 142–157, doi:10.1111/1475-4959.04976, http://dx.doi.org/10.1111/1475-4959.04976, 2003.

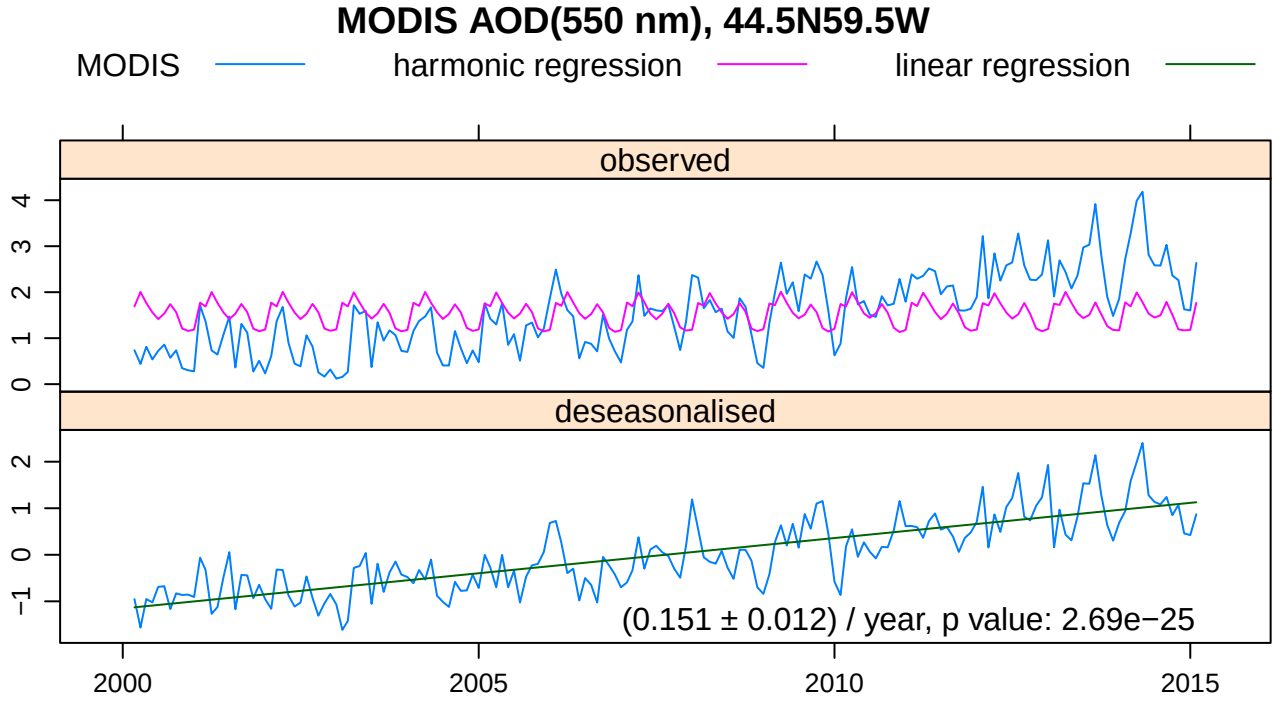

Figure S39. Same as Fig. 3, but for the one degree cell with the centre 44.5°N59.5°W in the Aral Sea region.

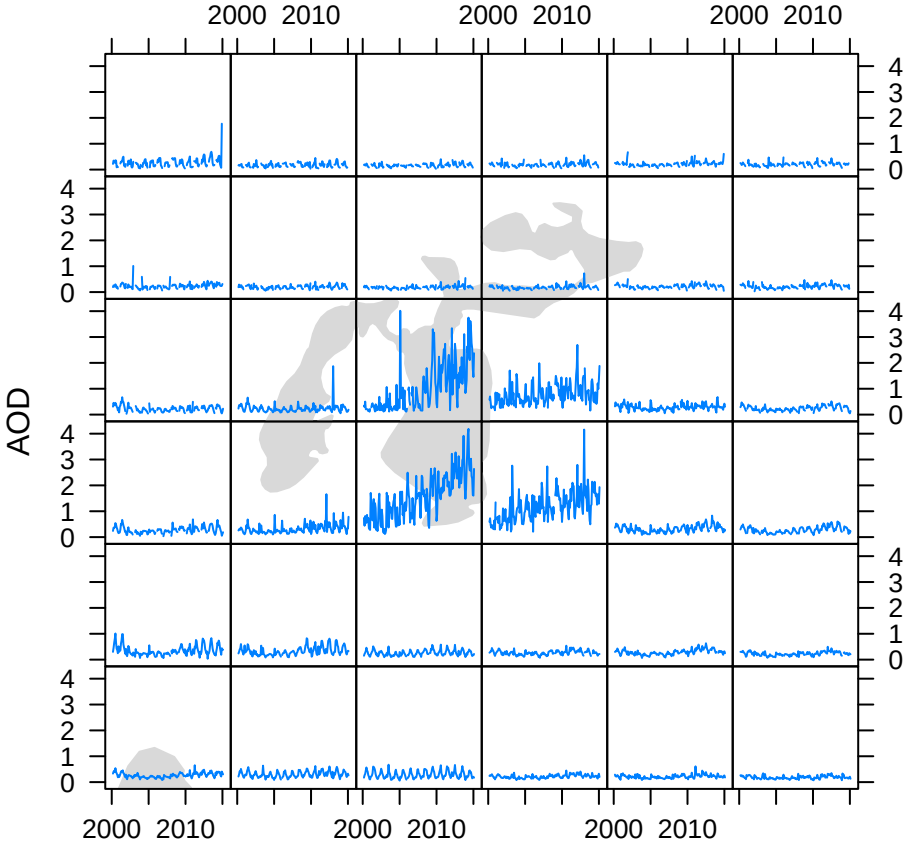

Figure S40. Each panel displays the 15 year AOD time series for a one degree grid cell the location of which is indicated by the grey silhouette showing the Aral Sea. Figure S39 corresponds to the third pixel in the fourth row. Some cells have incomplete monthly time series and therefore are not shown in Fig. 1.

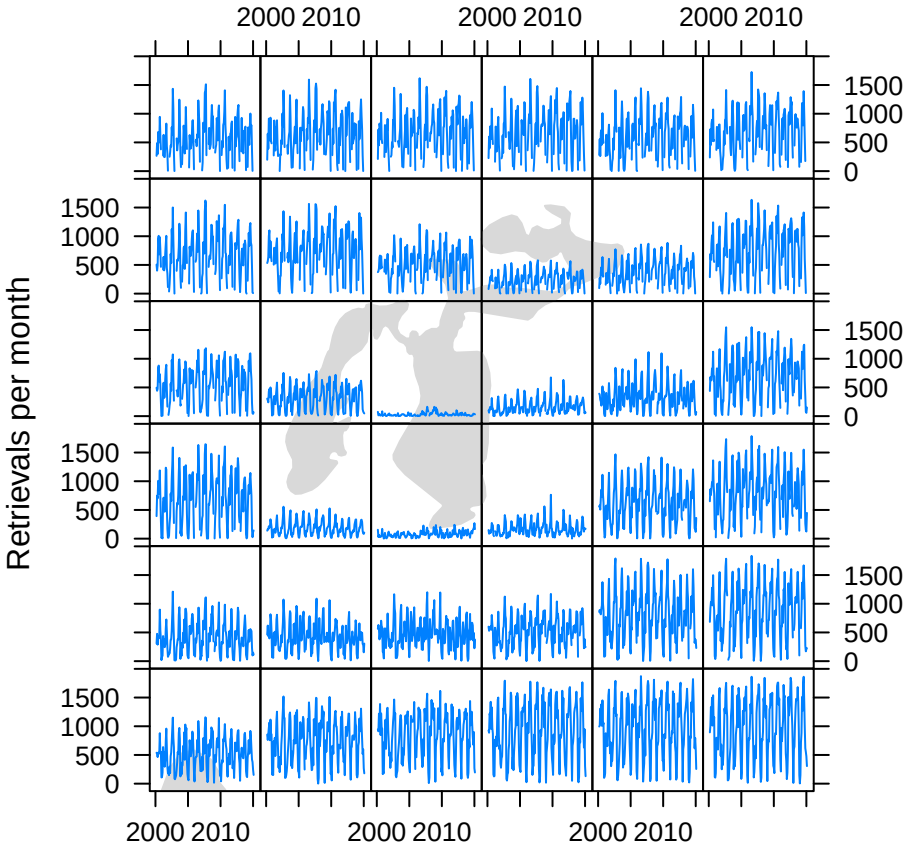

Figure S41. Same as Fig. S40 but showing the number of retrievals per month instead of the AOD.

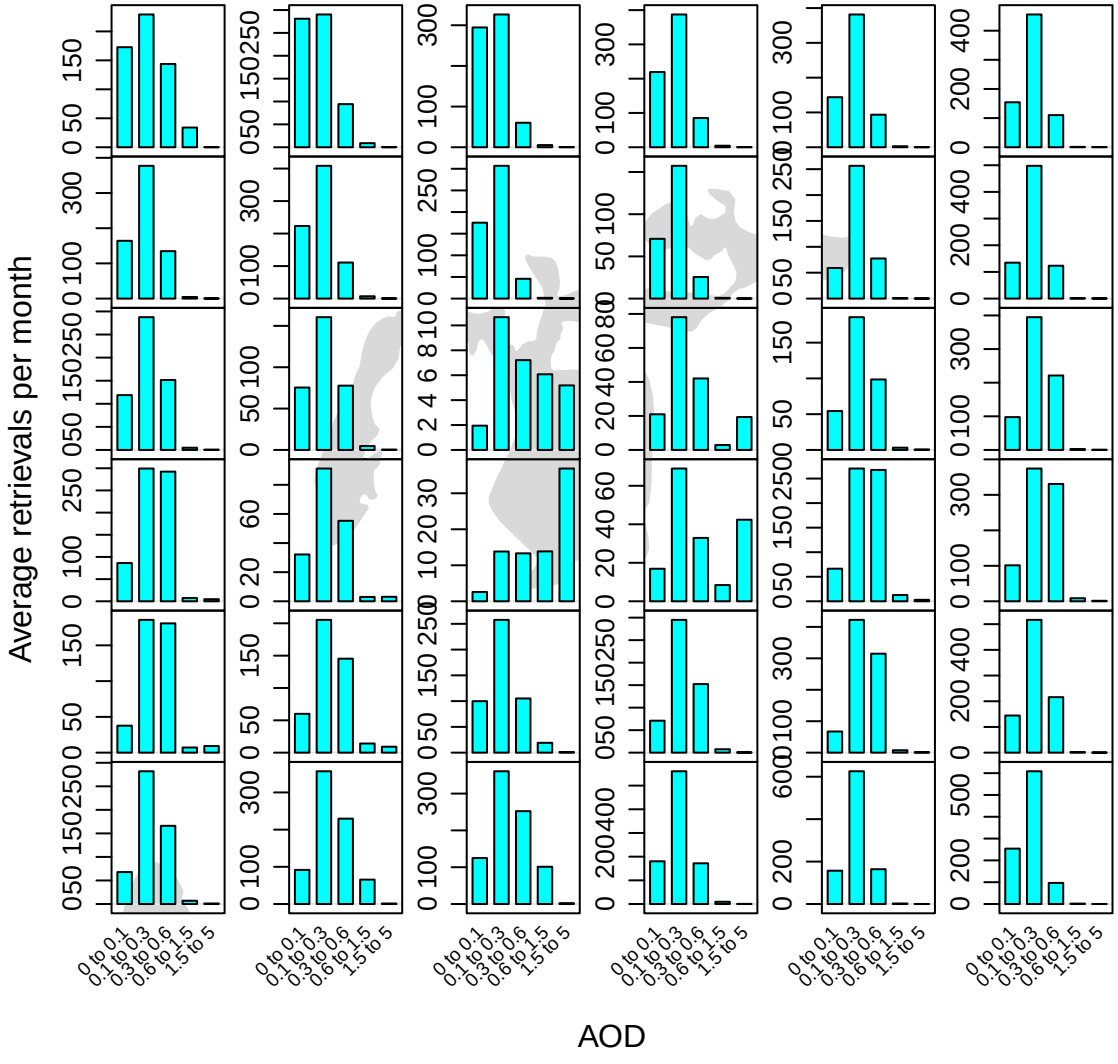

Figure S42. 15 year averages of the monthly AOD histograms. Each panel shows the histogram for the one degree grid cell the location of which is indicated by the grey silhouette showing the Aral Sea.

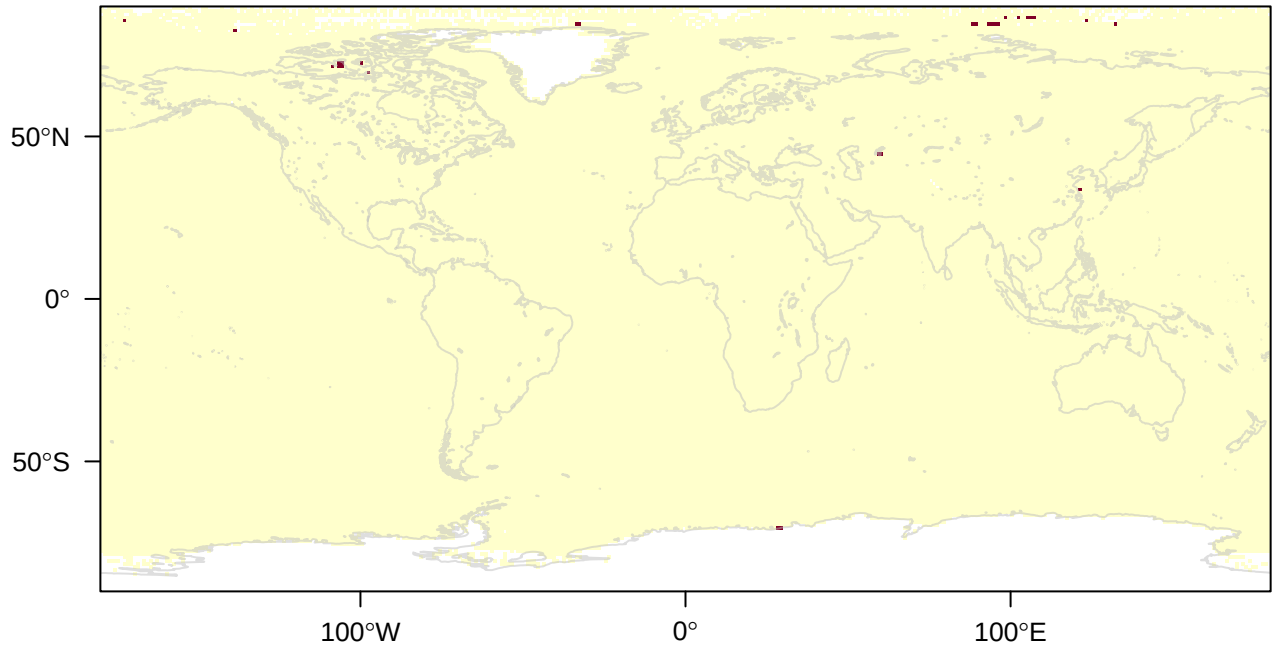

Figure S43. In light yellow grid cells the frequency of high AOD values above 1.5 is smaller than the average frequency of the AOD bins 0 to 0.1, 0.1 to 0.3, 0.3 to 0.6, 0.6 to 1.5 and 1.5 to 5. In dark red cells this condition is not fulfilled, which raises the suspicion that the retrievals over these regions are unreliable and gives reason to not consider them for further analysis.

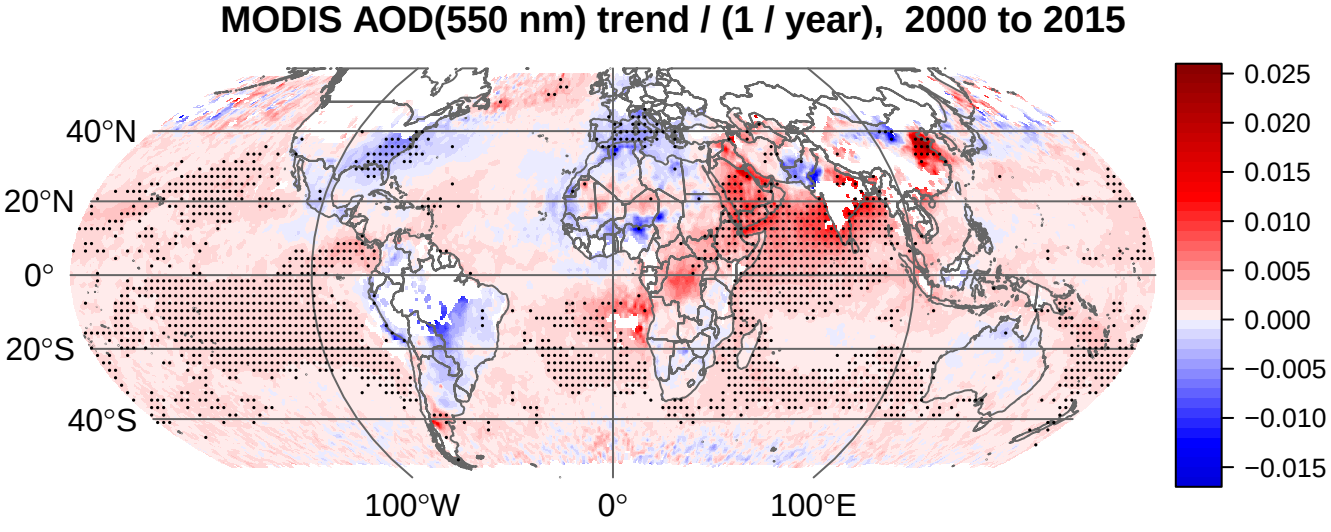

Figure S44. As Fig. 1, but after applying the filter shown in Fig. S43.